NASA TECHNICAL MEMORANDUM

NASA TM X-3261

NASA TM X-3261

REAL-TIME SIMULATION OF F100-PW-100 TURBOFAN ENGINE USING THE HYBRID COMPUTER

John R. Szuch and Kurt Seldner

Lewis Research Center

Cleveland, Ohio 44135

NATIONAL AERONAUTICS AND SPACE ADMINISTRATION • WASHINGTON, D. C. • AUGUST 1975

1. Report No.	2. Government Accession No.	3. Recipient's Catalog No.
NASA TM X-3261		

4. Title and Subtitle	5. Report Date
REAL-TIME SIMULATION OF F100-PW-100 TURBOFAN ENGINE USING THE HYBRID COMPUTER	AUGUST 1975
	6. Performing Organization Code
7. Author(s)	8. Performing Organization Report No.
John R. Szuch and Kurt Seldner	E-8136
	10. Work Unit No.
9. Performing Organization Name and Address	505-04
Lewis Research Center National Aeronautics and Space Administration Cleveland, Ohio 44135	11. Contract or Grant No.
	13. Type of Report and Period Covered
12. Sponsoring Agency Name and Address	Technical Memorandum
National Aeronautics and Space Administration Washington, D.C. 20546	14. Sponsoring Agency Code

15. Supplementary Notes

16. Abstract

A real-time hybrid computer simulation of the F100-PW-100 augmented turbofan has been developed. The simulation is intended to support controls research programs involving that engine. The digital portion of the hybrid computer was used primarily to perform the bivariate function generation associated with modeling the performance of the engine's rotating components. The remaining calculations were performed on the analog computer. Steady-state simulation data are presented to show that the real-time simulation matches baseline digital simulation results over a wide range of power settings and flight conditions. Sea-level, static, transient data are presented to show that the real-time simulation matches the baseline digital simulation dynamics. Steady-state simulation data are compared with sea-level, experimental data to show that the real-time hybrid and baseline digital simulations do adequately predict the performance of the actual engine. FORTRAN listings and analog patching diagrams are provided.

17. Key Words (Suggested by Author(s))	18. Distribution Statement
Simulation; Hybrid computer; Turbofan; Real time; Transient; Dynamics	Unclassified - unlimited STAR category 07 (rev.)

19. Security Classif. (of this report)	20. Security Classif. (of this page)	21. No. of Pages	22. Price*
Unclassified	Unclassified	80	$4.75

* For sale by the National Technical Information Service, Springfield, Virginia 22151

CONTENTS

REAL-TIME SIMULATION OF F100-PW-100 TURBOFAN ENGINE USING THE HYBRID COMPUTER

by John R. Szuch and Kurt Seldner

Lewis Research Center

SUMMARY

This report describes the development of a real-time hybrid computer simulation of the F100-PW-100 augmented turbofan. The simulation is intended to support controls research programs involving that engine. The F100-PW-100 real-time simulation was modeled after a similar simulation of the TF30-P-3 turbofan engine. The F100-PW-100 real-time simulation has both wide-range steady-state and transient computing capabilities. Factors such as fluid momentum, mass and energy storage, and rotor inertias are included. The digital portion of the hybrid computer was used primarily to perform the bivariate function generation associated with modeling the performance of the engine's rotating components. The remaining calculations (including integration) were performed by the analog portion of the hybrid computer.

Both steady-state and transient data were generated with the real-time engine simulation. An analog simulation of the engine's hydromechanical fuel control and a digital simulation of the engine's electronic supervisory control were used to control the simulated engine over a wide range of power settings and flight conditions. Resultant steady-state data were compared with similar data obtained with the engine manufacturer's baseline digital simulation of the engine and controls. The results of the comparison show that the real-time simulation results do adequately match the baseline digital steady-state results over the flight envelope. The responses of both the real-time hybrid and baseline digital simulated engines to rapid movements of the power lever were compared at sea-level static conditions. The results of that comparison indicate that the real-time simulation does adequately match the baseline digital simulation in predicting the transient behavior of the engine. Steady-state simulation data were compared with sea-level, static experimental data. The results of this comparison indicate that both the baseline digital and real-time hybrid simulations of the F100-PW-100 engine do adequately predict the performance of the actual engine.

INTRODUCTION

In recent years, there has been increased interest in developing digital, electronic controls for airbreathing propulsion systems (ref. 1). The use of a digital computer, with its inherent precision and its logic and memory capabilities, will provide the propulsion system control with more flexibility and versatility than is currently provided by hydromechanical controls. The increased flexibility and versatility are necessary to allow engines and inlets to operate at higher levels of performance over a wider range of flight conditions. The use of digital controls can also reduce pilot workloads, improve control maintainability, and reduce control complexity and weight.

The development of digital controls for turbojet and turbofan engines can be facilitated by the use of a real-time computer simulation of the engine (ref. 2). The engine simulation provides a "test bed" for evaluating new control laws and for checking and "debugging" the actual control software prior to engine testing. A real-time engine simulation enables the control developer to evaluate the timing and sequencing within the digital control and to predict the effects of extended digital sampling intervals (refs. 3 and 4) on engine performance.

Turbojet and turbofan engines may be simulated by using analog (ref. 5), digital (refs. 6 to 8), or hybrid (refs. 2, 9, and 10) computers. A real-time requirement usually limits the possible choices to the analog and hybrid computers. A purely analog simulation of a turbofan engine requires a large amount of computing equipment. Much of this equipment is needed to perform the function generation associated with modeling the performance of the engine's rotating components (fan, compressor (or compressors), and turbine (or turbines)). Large, all-analog simulations may also suffer from long setup and checkout times and a lower level of accuracy. The precision, repeatability, and memory capabilities of a hybrid computer can be used to perform the necessary function generation and also to aid in the setup and checkout of the analog portion of the simulation.

This report describes a real-time hybrid computer simulation of the Pratt & Whitney F100-PW-100 augmented turbofan engine. The simulation has both steady-state and transient calculation capabilities and is intended for supporting controls research programs involving that engine. The mathematical model of the engine was implemented on the Lewis Research Center's Electronic Associates Incorporated (EAI) Hybrid Computer System. This system consists of a Model 640 Digital Computer, a Model 680 Analog Computer, and a Model 681 Analog Computer. The mathematical model was patterned after the engine manufacturer's digital (baseline) simulation of the engine. Many of the assumptions and techniques employed in the development of the F100-PW-100 real-time simulation are based on experience gained while developing a similar real-time simulation of the Pratt & Whitney TF30-P-3 engine (ref. 2).

Results are presented which compare steady-state data from the real-time simulation with baseline digital simulation results over a wide range of power settings and flight conditions. Limited comparisons with transient results from the baseline digital simulation and with steady-state experimental data are also made. The report also includes the equations which model the engine, FORTRAN listings, and analog patching diagrams. Significant differences between the F100-PW-100 and TF30-P-3 real-time simulations are pointed out.

ENGINE DESCRIPTION

The Pratt & Whitney F100-PW-100 engine (fig. 1) is an axial, mixed-flow, augmented, twin-spool, low-bypass-ratio turbofan. A single inlet is used for both the fan airflow and the engine core airflow. Airflow leaving the fan is separated into two flow streams: one stream passing through the engine core and the other stream passing through the annular fan duct. A three-stage fan is connected by a through-shaft to the two-stage, low-pressure turbine. A 10-stage compressor is connected by a hollow shaft to the two-stage, high-pressure turbine. The fan has variable, trailing-edge, inlet guide vanes. The inlet guide vanes are positioned by the engine's electronic supervisory control system as a function of fan corrected speed to maintain fan stability at low speeds. The compressor has a variable inlet guide vane followed by two variable stator vanes. The compressor vanes are positioned by the engine's hydromechanical fuel control system as a function of compressor corrected speed. Engine airflow bleed is extracted at the compressor exit and discharged through the fan duct during starting. Compressor discharge bleed air is also used to cool the high- and low-pressure-turbine blades and to power the augmentor turbopump.

The main combustor consists of an annular diffuser and a chamber with 16 fuel nozzles. The hydromechanical fuel control system meters fuel to the main combustor as a function of the power lever angle PLA, the compressor speed N_H, the fan discharge total temperature T_{13}, and the compressor discharge static pressure $P_{s,3}$. (All symbols are defined in appendix A. Numerical subscripts refer to locations in the engine (fig. 1).)

The engine core and fan duct streams combine in an augmentor and are discharged through a variable convergent-divergent nozzle. The augmentor consists of a diffuser section and five concentric fuel manifolds (zones). The hydromechanical augmentor fuel control meters fuel to the five zones as a function of PLA, T_{13}, and $P_{s,3}$. The nozzle area is controlled so as to maintain a desired engine airflow during augmented operation.

ENGINE MODEL

The mathematical model describing the performance of the F100-PW-100 engine is patterned after the engine manufacturer's digital simulation (CCD 1015) of the engine. Wide-range, overall performance maps of the engine's rotating components are utilized so as to provide wide-range, steady-state accuracy, Factors such as fluid momentum, mass and energy storage, and rotor inertias are included so as to provide transient capability. However, in order to satisfy the real-time requirement and to minimize the amount of required analog equipment, nearly all fluid properties such as specific heats and gas constants are assumed to be constant.

Figure 2 contains a computational flow diagram of the F100-PW-100 real-time simulation. It can be seen that the mathematical model consists of a number of individual elements and their related volumes (inlet, fan, compressor, etc.) each of which requires a number of input variables and generates one or more output variables. However, unlike a digital simulation, all calculations in the real-time hybrid simulation can be considered to be performed in parallel. Descriptions of the individual element models are provided in appendix B. Appendix B also contains a complete list of equations defining the F100-PW-100 real-time simulation model. Differences between the F100-PW-100 and TF30-P-3 (ref. 2) models are pointed out.

HYBRID SIMULATION

The equations describing the F100-PW-100 mathematical model were implemented on the Lewis Research Center's Hybrid Computing System. This system consists of an EAI Model 640 Digital Computer, a Model 680 Analog Computer, and a Model 681 Analog Computer. The split of the computation load between the digital and analog computers was similar to that employed in the TF30-P-3 simulation (ref. 2). That is, the digital computer was used primarily to perform the bivariate function generation associated with modeling the performance of the engine's rotating components. In addition to this function generation, the digital computer also performed the calculations required to compute the engine thrust. In order to minimize the core storage requirement and the digital update time while allowing the use of FORTRAN programming, scaled-fraction (ref. 2) variables and arithmetic routines were used in the main digital computational loop. Scaled-fraction variables may not exceed unity and are represented by a single 16-bit word on the EAI 640 Digital Computer. The need to limit the digital update time to a small value (~5 msec) to guarantee stability when operating the simulation in real time prevented a fuller use of the digital computing capability. Appendix C contains a FORTRAN listing of the digital portion of the F100-PW-100 real-time simulation. Reference 2 includes a discussion of the digital function generation programs MAP2 and

MAP2L, which are used in both the TF30-P-3 and F100-PW-100 simulations. The digital portion of the F100-PW-100 real-time simulation required 11 741 words of core storage and had an update time of 6.37 milliseconds with constant values for the input variables.

The remaining calculations were performed on the analog computers. The analog computers performed all the operations characteristics of analog computers (i.e., summing, integration with respect to time, multiplication, attenuation, univariate function generation, etc.). The use of peripheral equipment such as x-y plotters and strip-chart recorders allowed continuous monitoring by the user of computed variables. The split of the computation load between the two analog consoles was based on the computing equipment limitations of each console. For example, the full complement of 24 multipliers on the 680 Analog Computer and 30 multipliers on the 681 Analog Computer was utilized. In addition, the full complement of six digital-analog multipliers (DAM's) on the 680 Analog Computer was used. Appendix D contains the analog patching diagrams and potentiometer settings for the F100-PW-100 real-time simulation.

RESULTS AND DISCUSSION

The usefulness of a simulation such as the F100-PW-100 real-time simulation depends on its ability to accurately represent the physical system over the desired range of operation. The F100-PW-100 real-time simulation should match the steady-state and transient engine performance for power settings from idle to full-augmentation at altitudes and flight speeds within the envelope shown in figure 3. Figure 3 also shows the flight conditions selected for comparison of hybrid and baseline digital data.

The following sections compare both steady-state and transient data obtained with the F100-PW-100 real-time simulation with the corresponding baseline digital data. The validity of both the hybrid and baseline digital simulations is demonstrated by comparing steady-state simulation data with available experimental data.

Steady-State Simulation Results

Comparison with baseline digital data. - The F100-PW-100 real-time simulation was operated in an open-loop fashion at each of the flight conditions shown in figure 3. Open-loop operation was selected to allow any engine-related errors to be isolated from control-related errors. For all open-loop runs, the five input variables to the simulation ($\dot{w}_{F,4}$, $\dot{w}_{F,7}$, A_7, GVIPOS, and HVSPOS) were set to the values obtained from the baseline digital simulation at the flight condition and power setting of interest. This provided a basis of comparison between hybrid and baseline digital data. The engine

variables selected for comparison were compressor speed, fan speed, main-combustor pressure, high-pressure-turbine inlet temperature, fan airflow, fan-tip pressure ratio, and nozzle inlet temperature. Agreement between hybrid and baseline digital values for all these variables implies agreement for almost all other engine variables. For convenience, engine variable data were plotted against power lever angle.

Figures 4 to 10 show the effects of flight condition on the match of hybrid and baseline digital steady-state data. Since the "design" point for the hybrid simulation was the sea-level, static, military-power (PLA = 73°) condition, the agreement between hybrid and baseline digital data at this condition was expected. Therefore, the validity of the mathematical model used in the hybrid simulation depends on the match of hybrid and baseline digital data at part-power settings and/or non-sea-level, static conditions.

Figures 4 and 5 compare the hybrid and baseline digital simulation values of compressor and fan speeds, respectively. Good agreement between rotor speeds at part-power settings for all flight conditions was observed. The observed disagreement between fan speeds during non-sea-level, static augmentation (PLA $> 80^{\circ}$) may be attributed to differences in the hybrid and baseline digital models of the nozzle. The assumption of constant, nozzle inlet, specific-heat ratio in the hybrid simulation would contribute to the errors in fan speed, which amount to about 4 percent of the design value.

Figures 6 and 7 compare the hybrid and baseline digital simulation values of main-combustor pressure and high-pressure-turbine inlet temperature, respectively. The observed agreement in pressure and temperature over the range of power settings and flight conditions substantiates the steady-state models of the fan hub, compressor, and main combustor used in the hybrid simulation.

Figures 8 and 9 compare the hybrid and baseline digital simulation values of fan airflow and fan-tip pressure ratio, respectively. Some discrepancies in both airflow and pressure ratio were observed at the altitude conditions. These discrepancies may be due to a combination of (1) no Reynolds number effects on fan performance in the hybrid simulation and (2) the aforementioned differences in the nozzle models at non-sea-level, static conditions. The observed discrepancies in fan airflow and fan-tip pressure ratio at high altitudes amount to approximately 3 percent of the corresponding design values.

Figure 10 compares the hybrid and baseline digital simulation values of the nozzle inlet temperature. Reasonable agreement was observed over the range of power settings and flight conditions. The observed differences in nozzle inlet temperature at the highest altitude conditions may be attributed to the assumption of constant specific heats in the hybrid computer model of the augmentor.

Comparison with experimental data. - In general, figures 4 to 10 indicate that the hybrid simulation does adequately match the baseline digital simulation in representing the steady-state behavior of the F100-PW-100 engine. The ability of both the hybrid and digital simulations to represent the actual engine performance, however, can only be demonstrated by comparing simulation data with experimental data. Steady-state,

experimental data obtained at sea-level, static conditions were available. Since the nonaugmented and augmented tests were run at different ambient temperatures, data from those tests were considered separately. The hybrid simulation was run with the appropriate inlet conditions to match the experimental tests. The controlled inputs to the simulation were provided by an analog simulation of the hydromechanical fuel control and a digital simulation of the electronic supervisory control. Because of a discrepancy between the experimental and simulated values of the power lever angle, comparisons of hybrid, baseline digital, and experimental data were made on the basis of equivalent main-combustor fuel flows (for nonaugmented tests) and augmentor fuel flows (for augmented tests).

Figure 11 compares simulation and experimental data for the nonaugmented tests. The excellent agreement in all engine variables indicates (1) that the baseline digital simulation does represent the actual engine sea-level static performance over the entire range of nonaugmented operation and (2) that the hybrid simulation does adequately match the baseline digital simulation.

Figure 12 compares simulation and experimental data for the augmented tests. Since most engine variables are held at their military-power values by the control during augmentation, the only significant variables to consider during augmentation are the nozzle inlet temperature and the nozzle area. Figure 12 indicates that the simulations do predict the correct nozzle inlet temperature resulting from the augmentor fuel flow. However, figure 12(b) shows that the actual engine control resulted in a larger nozzle area during augmentation than predicted by either simulation. Figure 12 indicates that the actual nozzle may have a lower flow coefficient than predicted by the baseline digital simulation.

Transient Simulation Results

The preceding sections have demonstrated the ability of the F100-PW-100 real-time hybrid simulation to predict the steady-state performance of the actual engine. If the simulation is to serve as a useful tool in developing digital control systems for the engine, it must also be capable of predicting transient engine performance. A comparison of hybrid and baseline digital transient data was limited to sea-level, static conditions because additional baseline digital data were not available.

The hybrid simulation was operated with the five control inputs scheduled as functions of time to match the baseline digital values for a power lever ramp from idle to military power in 0.5 second. As in the case of the steady-state comparison of simulation results, open-loop operation was selected for the transient comparison to isolate any simulation errors from errors associated with the control implementation.

Figure 13(a) shows a comparison of the hybrid and baseline digital simulation responses of the main-combustor pressure. The hybrid simulation response was more rapid than the digital response. Similar results were obtained with the real-time hybrid simulation of the TF30-P-3 engine (ref. 2). In that instance, the gain of the main-combustor integrator was decreased by a factor of 25 to match baseline digital data. This decrease, in effect, accounted for heat-transfer effects in the main combustor, which were not included in the hybrid model. Figures 13(b) and (c) show the effect of reducing this gain on the hybrid simulation response of the F100-PW-100 main-combustor pressure. A reduction factor of 20 was selected for subsequent transient tests.

Figure 14 shows a comparison of the responses of hybrid and baseline digital simulation engine variables to the simulated idle-to-military power lever "slam." As previously noted, the main-combustor pressure gain was reduced by a factor of 20 for this test. Also, the scheduled values of exhaust nozzle area correspond here to an "idle-area-reset on" condition. That is, the exhaust nozzle is near its maximum opening at idle and is scheduled closed by the hydromechanical control as a function of a rate-limited power lever angle as the engine accelerates. Figure 14 shows excellent agreement in all engine variables.

Figure 15 shows a comparison of hybrid and baseline digital simulation variables for a simulated power lever cycle from military to maximum augmentation to military. As in the case of the idle-to-military power lever transient, the scheduled values for the control inputs were determined from the baseline digital simulation. The function of the exhaust nozzle area control during augmentation is to maintain a constant flow impedance to the main engine while the main fuel control modulates fuel flow to the main combustor to maintain constant compressor speed. The results shown in figure 15 indicate that the scheduled values for the control inputs do result in a match of baseline digital and hybrid simulation values for rotor speeds, main-combustor pressure and temperature, and nozzle inlet temperature. However, the suspected shortcomings in the exhaust nozzle model did result in steady-state errors in the hybrid-simulated exhaust nozzle inlet pressure during maximum augmentation. No appreciable errors in the transient characteristics of these variables can be observed in this figure.

SUMMARY OF RESULTS

This report describes a real-time, hybrid computer simulation of the F100-PW-100 augmented turbofan. While the F100-PW-100 real-time simulation was modeled after the TF30-P-3 simulation, a number of modifications have been incorporated in an attempt to extend the range of accuracy. For example, temperature-sensitive specific heats are used in the calculations of fan and compressor torques. Steady-state simulation data are presented for a full range of power settings over the entire flight envelope. The

F100-PW-100 real-time simulation is shown to adequately match the baseline digital steady-state results over the entire flight envelope. Transient data are presented for sea-level, static conditions and are also shown to match digital results. Both hybrid and baseline digital steady-state data are compared with sea-level, static experimental data to show that the basic mathematical models used in the simulations are valid. These results indicate that the real-time simulation requirement can be satisfied while maintaining a sufficient degree of accuracy over a wide range of power settings and flight conditions.

With the simulation structure described in this report the digital computer update time was 6.37 milliseconds and resulted in stable, real-time operation. The use of a faster digital computer than the EAI Model 640 would, of course, allow more computations to be done in the digital computer during the 6- to 7-millisecond duration.

Lewis Research Center,
National Aeronautics and Space Administration,
Cleveland, Ohio, March 11, 1975,
505-04.

APPENDIX A

SYMBOLS

A	cross-sectional area, cm^2 ($in.^2$)
C_d	nozzle flow coefficient
c_p	specific heat at constant pressure, J/kg-K (Btu/lbm-^oR)
F	thrust, N (lbf)
FN7	nozzle flow function
f_i	functional relation, i = 1 to 11
f/a	local fuel-air ratio
GVIPOS	fan inlet guide vane position, deg
g_c	gravitational conversion factor, 100 cm-kg/N-sec^2 (386.3 lbm-in./lbf-sec^2)
HVF	heating value of fuel, J/kg (Btu/lbm)
HVSPOS	compressor stator vane position, deg
Δh	turbine enthalpy drop, J/kg (Btu/lbm)
hp	turbine map enthalpy drop parameter, J/kg-$K^{1/2}$-rpm (Btu/lbm-$^oR^{1/2}$-rpm)
I	polar moment of inertia, N-cm-sec^2 (ft-lbf-sec^2)
J	mechanical equivalent of heat, 100 N-cm/J (778.3 ft-lbf/Btu)
K_{AB}	augmentor pressure loss coefficient, N^2-sec^2/kg^2-cm^4-K (lbf^2-sec^2/lbm^2-$in.^4$-^oR)
K_B	main-combustor pressure loss coefficient, N^2-sec^2/kg^2-cm^4-K (lbf^2-sec^2/lbm^2-$in.^4$-^oR)
K_{BLWHT}	fraction of high-pressure-turbine cooling bleed that is performing work
K_{BLWLT}	fraction of low-pressure-turbine cooling bleed that is performing work
K_N	nozzle flow constant, kg-$K^{1/2}$/N-sec (lbm-$^oR^{1/2}$/lbf-sec)
K_{PR5}	low-pressure-turbine discharge pressure loss coefficient
ℓ	length, cm (in.)
M	Mach number
N	rotational speed, rpm
P	total pressure, N/cm^2 (psia)

P/P	pressure ratio
PLA	power lever angle, deg
P_s	static pressure, N/cm^2 (psia)
Q	torque, N-cm (in. -lbf)
R_A	gas constant of air, 44.83 N-cm/kg-K (640.1 in. -lbf/lbm-^oR)
T	total temperature, K (^oR)
T/T	temperature ratio
t	time, sec
V	volume, cm^3 ($in.^3$)
W	stored mass, kg (lbm)
$\dot{w}$	mass flow rate, kg/sec (lbm/sec)
$\dot{w}_c$	corrected mass flow rate, kg/sec (lbm/sec)
$\dot{w}_p$	turbine map flow parameter, kg-K-cm^2/N-rpm-sec (lbm-^oR-$in.^2$/lbf-rpm-sec)
γ	specific-heat ratio
δ	total pressure relative to sea-level conditions
η	efficiency
θ	total temperature relative to standard-day conditions
τ	time constant, sec

Subscripts:

AB	augmentor
B	main combustor
BLHT	high-pressure-turbine cooling bleed
BLLT	low-pressure-turbine cooling bleed
C	compressor
D	fan duct
e	nozzle exit plane
F	fuel
FAN	fan
H	high
HT	high-pressure turbine

I	inlet
ID	fan hub (core)
i	initial conditions
j	engine station (fig. 1); j = 0, 2, 2.1, 2.2, 3, 4.1, 5, 6, 7, 8, 13, 16
j'	entrance to volume at station j; j = 3, 4, 4.1, 6, 7, 13, 16
L	low
LT	low-pressure turbine
M	map
m	measured
N	nozzle
n	net
OD	fan tip (bypass)
SUB	subsonic
SUP	supersonic
TPBL	turbopump bleed

APPENDIX B

ENGINE MODEL

This appendix describes the significant features of the individual elements which comprise the F100-PW-100 engine model shown in figure 2. Emphasis is placed on noting the differences between the F100-PW-100 model and the TF30-P-3 model described in reference 2.

Inlet

The mathematical treatment of the inlet in the F100-PW-100 real-time simulation is identical to that used in reference 2. A steady-state representation of a typical inlet recovery is used to provide the proper fan inlet conditions (P_2, T_2) for a specific flight condition (P_0, T_0, M_0). The following equations define the inlet model in the F100-PW-100 real-time simulation:

$$\left(\frac{T}{T}\right)_I = 1.0 + 0.2\, M_0^2 \tag{B1}$$

$$\left(\frac{P}{P}\right)_I = \left(\frac{T}{T}\right)_I^{3.5} \tag{B2}$$

$$\eta_I = 1.0 \quad \text{if } M_0 \leq 1.0$$

$$= 1.0 - 0.075(M_0 - 1.0)^{1.35} \quad \text{otherwise} \tag{B3}$$

$$T_2 = \left(\frac{T}{T}\right)_I T_0 \tag{B4}$$

$$P_2 = \left(\frac{P}{P}\right)_I P_0 \eta_I \tag{B5}$$

Fan

The mathematical treatment of the fan in the F100-PW-100 real-time simulation is quite similar to that discussed in reference 2. That is, overall performance maps (rather than individual stage data) are used, with separate performance maps for the tip (bypass) and hub (core) sections of the fan. Figure 16 shows the fan performance maps with the inlet guide vanes at their axial position. Since the fan's performance is affected by the inlet guide vanes, the data shown in figure 16 must be adjusted for nonaxial inlet guide vane positions. Based on data from the baseline digital simulation, the effect of the variable inlet guide vanes was accounted for by multiplying the map value of the corrected airflow (fig. 16(a)) by a linear function of the inlet guide vane position to obtain the actual fan corrected airflow. The effect of the inlet guide vane position on the fan-hub performance (fig. 16(b)) was assumed to be negligible.

The baseline digital data also indicated that the fan-tip and fan-hub temperature ratios could be computed from piecewise linear functions of the corresponding pressure ratios. Three segments were required to fit each of the temperature-ratio - pressure-ratio curves. The use of the linear functions eliminates the need for the bivariate function generation and exponentiation associated with using isentropic efficiency maps. The fan efficiency (hence, temperature ratios) was assumed to be unaffected by changes in the inlet guide vane position. The following equations define the fan model in the F100-PW-100 real-time simulation:

$$(\dot{w}_c)_{FAN,M} = f_1\left(\frac{P_{13}}{P_2}, \frac{N_L}{\sqrt{\theta_2}}\right) \tag{B6}$$

$$\left(\frac{P}{P}\right)_{FAN,ID} = f_2\left(\frac{P_{13}}{P_2}, \frac{N_L}{\sqrt{\theta_2}}\right) \tag{B7}$$

$$\dot{w}_2 = (\dot{w}_c)_{FAN,M} \frac{\delta_2(1.0143 + 0.002653\ \mathrm{GVIPOS})}{\sqrt{\theta_2}} \tag{B8}$$

$$P_{2.1} = P_{2.2} = \left(\frac{P}{P}\right)_{FAN,ID} P_2 \tag{B9}$$

$$\left(\frac{T}{T}\right)_{FAN,OD} = 0.1833 \frac{P_{13}}{P_2} + 0.9029 \quad \text{if} \quad \frac{P_{13}}{P_2} \geq 1.85$$

$$= 0.2533 \frac{P_{13}}{P_2} + 0.7733 \quad \text{if} \quad 1.4 \leq \frac{P_{13}}{P_2} < 1.85$$

$$= 0.3200 \frac{P_{13}}{P_2} + 0.6800 \quad \text{otherwise} \tag{B10}$$

$$T_{13'} = \left(\frac{T}{T}\right)_{FAN,OD} T_2 \tag{B11}$$

$$\left(\frac{T}{T}\right)_{FAN,ID} = 0.1603 \left(\frac{P}{P}\right)_{FAN,ID} + 0.9391 \quad \text{if} \left(\frac{P}{P}\right)_{FAN,ID} \geq 2.04$$

$$= 0.2198 \left(\frac{P}{P}\right)_{FAN,ID} + 0.8177 \quad \text{if} \quad 1.48 \leq \left(\frac{P}{P}\right)_{FAN,ID} < 2.04$$

$$= 0.2979 \left(\frac{P}{P}\right)_{FAN,ID} + 0.7021 \quad \text{otherwise} \tag{B12}$$

$$T_{2.1} = T_{2.2} = \left(\frac{T}{T}\right)_{FAN,ID} T_2 \tag{B13}$$

The primed station designations (e.g., 13') refer to the entrance to the volume.

Compressor

The F100-PW-100 real-time compressor model differs from the compressor model described in reference 2 in a number of respects. While both models use overall performance maps, the F100-PW-100 compressor model uses pressure ratio (rather than corrected airflow) as an input variable (fig. 2). This eliminates the need for an external calculation of the airflow. Figure 17 shows the F100-PW-100 compressor performance with the stator vanes at their axial position. As in the case of the fan, the performance of the compressor was affected by the variable stator vanes. Based on baseline digital

data, the effect of the variable stator vanes was accounted for by adjusting the map value of the corrected airflow with a bivariate function of the stator vane position and compressor corrected speed. Figure 18 shows the effect of variable stator vane position on the compressor performance map.

The F100-PW-100 compressor temperature ratio was fit by a two-segment linear function of the compressor pressure ratio. The compressor efficiency (hence, temperature ratio) was assumed to be unaffected by changes in the stator vane position. The following equations define the F100-PW-100 real-time compressor model:

$$(\dot{w}_c)_{c,m} = f_3\left(\frac{P_3}{P_{2.2}}, \frac{N_H}{\sqrt{\theta_{2.2}}}\right) \tag{B14}$$

$$\dot{w}_{2.2} = (\dot{w}_c)_{C,m} \frac{\delta_{2.2}}{\left[1. + f_4\left(\frac{N_H}{\sqrt{\theta_{2.2}}}, \text{HVSPOS}\right)\right]\sqrt{\theta_{2.2}}} \tag{B15}$$

$$\left(\frac{T}{T}\right)_C = 0.0702 \frac{P_3}{P_{2.2}} + 1.3814 \quad \text{if } \frac{P_3}{P_{2.2}} \geq 5.75$$

$$= 0.1018 \frac{P_3}{P_{2.2}} + 1.1996 \quad \text{otherwise} \tag{B16}$$

$$T_{3'} = \left(\frac{T}{T}\right)_C T_{2.2} \tag{B17}$$

Engine Bleeds

The extraction of turbine cooling and augmentor turbopump bleeds from the compressor discharge is accounted for in the F100-PW-100 real-time simulation. All bleed flows were assumed to be proportional to the compressor inlet airflow. For convenience, the flow loss due to compressor seal leakage was lumped with the low-pressure-turbine cooling bleed. The following equations define the engine bleed model in the F100-PW-100 real-time simulation:

$$\dot{w}_{BLHT} = 0.1162\, \dot{w}_{2.2} \tag{B18}$$

$$\dot{w}_{BLLT} = 0.03828\,\dot{w}_{2.2} \tag{B19}$$

$$\dot{w}_{TPBL} = 0.00353\,\dot{w}_{2.2} \tag{B20}$$

Turbines

The mathematical models describing the performance of the F100-PW-100 turbines are identical to those described in reference 2. The overall performance of each turbine is described by a pair of bivariate functions. Figures 19 and 20 are performance maps showing the turbine flow and enthalpy drop parameters for the high- and low-pressure turbines, respectively. The cooling bleed for each turbine was assumed to reenter the flow stream at the discharge of the turbine, although a proportion of each bleed was assumed to perform turbine work. The following equations define the turbine models in the F100-PW-100 real-time simulation:

$$(\dot{w}_p)_{HT} = f_5\left(\frac{P_{4.1}}{P_4},\ \frac{N_H}{\sqrt{T_4}}\right) \tag{B21}$$

$$\dot{w}_4 = (\dot{w}_p)_{HT}\,\frac{P_4 N_H}{T_4} \tag{B22}$$

$$(hp)_{HT} = f_6\left(\frac{P_{4.1}}{P_4},\ \frac{N_H}{\sqrt{T_4}}\right) \tag{B23}$$

$$(\Delta h)_{HT} = (hp)_{HT}\sqrt{T_4}\,N_H \tag{B24}$$

$$(\dot{w}T)_{4.1'} = \dot{w}_4\left[\frac{c_{p,4}T_4}{c_{p,4.1}} - \frac{(\Delta h)_{HT}}{c_{p,4.1}}\right] + \dot{w}_{BLHT}\left[\frac{c_{p,3}T_3}{c_{p,4.1}} - \frac{K_{BLWHT}(\Delta h)_{HT}}{c_{p,4.1}}\right] \tag{B25}$$

$$(\dot{w}_p)_{LT} = f_7\left(\frac{P_5}{P_{4.1}},\ \frac{N_L}{\sqrt{T_{4.1}}}\right) \tag{B26}$$

$$\dot{w}_{4.1} = (\dot{w}_p)_{LT}\,P_{4.1}\,\frac{N_L}{T_{4.1}} \tag{B27}$$

$$(hp)_{LT} = f_8\left(\frac{P_5}{P_{4.1}}, \frac{N_L}{\sqrt{T_{4.1}}}\right) \tag{B28}$$

$$(\Delta h)_{LT} = (hp)_{LT}\sqrt{T_{4.1}}\, N_L \tag{B29}$$

$$(\dot{w}T)_{6'} = \frac{\dot{w}_{13}c_{p,16}T_{16}}{c_{p,6}} + \dot{w}_{4.1}\left[\frac{c_{p,4.1}T_{4.1}}{c_{p,6}} - \frac{(\Delta h)_{LT}}{c_{p,6}}\right] + \dot{w}_{BLLT}\left[\frac{c_{p,3}T_3}{c_{p,6}} - \frac{K_{BLWLT}(\Delta h)_{LT}}{c_{p,6}}\right] \tag{B30}$$

Table I lists the design parameters (specific heats, K_{BLWHT}, K_{BLWLT}, etc.) used in the real-time simulation of the F100-PW-100 engine.

Main Combustor and Augmentor

The only significant difference between the F100-PW-100 real-time main-combustor model and that described in reference 2 is the elimination of the high-frequency flow dynamics that were included in the TF30-P-3 simulation. The elimination of the main-combustor flow dynamics resulted in the need for a direct calculation of the main-combustor airflow from the instantaneous pressure drop across the main combustor. A simple energy balance was used to compute the steady-state temperature rise in the F100-PW-100 main combustor. However, in order to match baseline digital data over the full range of power settings, it was necessary to include a temperature-sensitive energy release from the injected fuel. The combined effects of temperature on the main-combustor efficiency and the heating value of the fuel were achieved with a linear function of the main-combustor temperature. The following equations define the main-combustor model in the F100-PW-100 real-time simulation:

$$\dot{w}_3 = \sqrt{\frac{P_3(P_3 - P_4)}{K_B T_3}} = \sqrt{\frac{R_A W_3(P_3 - P_4)}{K_B V_3}} \tag{B31}$$

$$(\dot{w}T)_{4'} = \frac{c_{p,3}}{c_{p,4}}\dot{w}_3 T_3 + \eta_B \frac{HVF}{c_{p,4}}\dot{w}_{F,4} \tag{B32}$$

$$\eta_B \frac{HVF}{c_{p,4}} = 49\ 602 - 7.3376\ T_4 \tag{B33}$$

The most significant difference between the F100-PW-100 and TF30-P-3 real-time augmentor models is the mixing of the core and duct flows at the augmentor entrance in the F100-PW-100 real-time simulation. While both real-time simulations assume a static pressure balance at this point in the engine, the TF30-P-3 real-time hybrid model (ref. 2) assumes no flow mixing and treats the core and duct sections of the augmentor and the nozzle as separate elements.

In order to match F100-PW-100 baseline digital data, the effective augmentor efficiency was fit by a piecewise linear function of the fuel-air ratio. Figure 21 shows the augmentor efficiency required to match the baseline digital data. The following equations define the augmentor model in the F100-PW-100 real-time simulation:

$$P_{16} = P_6 \tag{B34}$$

$$P_5 = K_{PR5} P_6 \tag{B35}$$

$$P_{7'} = P_6 - K_{AB} \dot{w}_6^2 \frac{T_6}{P_6} = P_6 - \frac{K_{AB} V_6 \dot{w}_6^2}{R_A W_6} \tag{B36}$$

$$(\dot{w}T)_{7'} = \frac{c_{p,6}}{c_{p,7}} \dot{w}_6 T_6 + \eta_{AB} \frac{HVF}{c_{p,7}} \dot{w}_{F,7} \tag{B37}$$

$$\eta_{AB} = f_9 \left[\left(\frac{f}{a} \right)_7 \right] \tag{B38}$$

$$\left(\frac{f}{a} \right)_7 = \frac{\dot{w}_{F,7}}{\dot{w}_6 - \dot{w}_{F,4}} \tag{B39}$$

Duct

The F100-PW-100 real-time duct model is essentially the same as the model described in reference 2. However, the steady-state duct pressure drop has been functionally related to the duct airflow (corrected to the duct discharge conditions) in the F100-PW-100 simulation. Figure 22 shows the duct pressure loss characteristic. As in the case of the TF30-P-3 simulation, the temperature rise (or drop) in the F100-PW-100 duct has been neglected. The following equations define the F100-PW-100 real-time duct model:

$$P_{16'} = P_{13}\left[1 - f_{10}\left(\frac{\dot{w}_{13}\sqrt{T_{16}}}{P_{16}}\right)\right] \tag{B40}$$

$$c_{p,16}T_{16} = c_{p,13}T_{13} \tag{B41}$$

Exhaust Nozzle

As in the case of the augmentor models, the F100-PW-100 and TF30-P-3 exhaust nozzle models differ with regard to the mixing of core and duct flow streams. Because of the assumed mixing of streams in the F100-PW-100 augmentor, only one nozzle model is required.

Because of the complexity involved in computing both subsonic and supersonic flows in a convergent-divergent nozzle, certain approximations and correction factors were employed in calculating the F100-PW-100 nozzle flow. The flow was calculated as if the nozzle were a convergent-only design. The resulting error in flow was compensated for by the use of a variable nozzle flow coefficient. In order to match baseline digital data (nonaugmented), a two-segment linear function of the nozzle pressure ratio was employed. In addition, a temperature-sensitive reduction in the effective nozzle throat area was used to match baseline data for augmented operation. Figure 23 shows the required nozzle area reduction. This area reduction was fit by four linear functions of the nozzle inlet temperature.

Since it was desirable to have a nozzle thrust calculation in the F100-PW-100 real-time simulation, it was necessary to account for the effects of the divergent nozzle on the exhaust-plane static pressure. Based on available digital data, the expansion ratio of the nozzle was fit by a quadratic function of the variable nozzle throat area. Isentropic flow tables (ref. 11) were implemented by quadratic functions of the expansion ratio to allow a determination of the static pressure at the nozzle exit for both subsonic and supersonic flow in the nozzle. Ram drag effects on the engine net thrust were also included in the F100-PW-100 real-time simulation. The following equations define the F100-PW-100 exhaust nozzle model:

$$\left(\frac{P}{P}\right)_N = \frac{P_0}{P_7} \tag{B42}$$

$$FN7 = 0.2588 \quad \text{if} \left(\frac{P}{P}\right)_N \leq 0.53$$

$$= \left(\frac{P}{P}\right)_N^{0.7143} \sqrt{1 - \left(\frac{P}{P}\right)_N^{0.2857}} \quad \text{otherwise} \tag{B43}$$

$$C_{d,7} = 0.9394 + 0.0277 \left(\frac{P}{P}\right)_N \quad \text{if} \left(\frac{P}{P}\right)_N \leq 0.50$$

$$= 0.9010 + 0.1045 \left(\frac{P}{P}\right)_N \quad \text{otherwise} \tag{B44}$$

$$\dot{w}_7 = K_N P_7 (FN7) C_{d,7} \frac{\left[A_7 - f_{11}(T_7)\right]}{\sqrt{T_7}} \tag{B45}$$

$$f_{11} = 0.0 \quad \text{if} \quad T_7 < 787.8$$

$$= 0.28719\ T_7 - 226.2 \quad \text{if} \quad 787.8 \leq T_7 < 888.9$$

$$= 0.09784\ T_7 - 57.93 \quad \text{if} \quad 888.9 \leq T_7 < 1165$$

$$= 0.20032\ T_7 - 177.5 \quad \text{if} \quad 1165 \leq T_7 < 1496$$

$$= 0.30867\ T_7 - 339.5 \quad \text{if} \quad T_7 \geq 1496 \tag{B46}$$

$$\frac{A_8}{A_7} = 0.52152 + 3.16282\ A_7 - 2.9508\ A_7^2 \tag{B47}$$

$$\left(\frac{P}{P}\right)_{SUB} = 4.7317 \left(\frac{A_8}{A_7}\right) - 1.6486 \left(\frac{A_8}{A_7}\right)^2 - 2.5089 \tag{B48}$$

$$\left(\frac{P}{P}\right)_{SUP} = 4.7317 \left(\frac{A_8}{A_7}\right) + 1.6486 \left(\frac{A_8}{A_7}\right)^2 + 3.5655 \tag{B49}$$

$$\frac{P_{s,e}}{P_7} = \left(\frac{P}{P}\right)_N \quad \text{if} \left(\frac{P}{P}\right)_N \geq \left(\frac{P}{P}\right)_{SUB}$$

$$= \left(\frac{P}{P}\right)_{SUP} \quad \text{otherwise} \tag{B50}$$

$$F_8 = 53.265\ \dot{w}_7 \sqrt{T_7 \left[1 - \left(\frac{P_{s,e}}{P_7}\right)^{0.20319}\right]} \quad \text{if} \left(\frac{P}{P}\right)_N \geq \left(\frac{P}{P}\right)_{SUB}$$

$$= 53.265\ \dot{w}_7 \sqrt{T_7 \left[1 - \left(\frac{P_{s,e}}{P_7}\right)^{0.20319}\right]} - A_8(P_0 - P_{s,e}) \quad \text{otherwise} \tag{B51}$$

$$F_n = F_8 - 20.041\ \dot{w}_2 M_0 \sqrt{T_0} \tag{B52}$$

Engine Dynamics

The previous sections describe the steady-state performance of the various components which comprise the F100-PW-100 engine. However, a transient engine simulation must also account for the effects of fluid compressibility, fluid momentum, energy storage, and rotor inertias on the transient performance of the engine.

Intercomponent volumes were assumed at engine locations where either (1) gas dynamics were considered to be important or (2) gas dynamics were required to avoid the need for iterative solution of equations. In these volumes, the storage of mass and energy occurs. The dynamic forms of the continuity, energy, and state equations were solved for the stored mass, temperature, and pressure in each volume. When mixing of gases was not involved, a simple first-order lag form of the energy equation was used.

The effects of fluid momentum on the transient behavior of the F100-PW-100 engine were considered only in the fan duct and augmentor tailpipe. The contribution of flow dynamics in the compressor, main combustor, and turbines was assumed to be primarily high frequency (>10 Hz) in nature and was consequently ignored.

The most significant factors in determining the transient behavior of a turbofan engine are the rotor moments of inertia. Rotor speeds were computed from the dynamic form of the angular momentum equation.

A comparison of hybrid and baseline digital data at low power settings indicated that the assumption of constant fluid properties in the hybrid simulation can lead to simulation

errors. Similar results were noted in reference 2. Therefore, the calculation of the F100-PW-100 compressor torque requirement was expanded to include a temperature-sensitive specific heat at the compressor discharge. A linear function of temperature was found to give a good match of hybrid and baseline digital data along the sea-level, static operating line. For other flight conditions, the intercept of the compressor discharge specific-heat function and the time-invariant fan discharge (hub) specific heat were adjusted to match baseline rotor speeds at the military power setting. The following equations define the dynamics in the F100-PW-100 real-time simulation:

$$W_3 = \int_0^t (\dot{w}_{2.2} - \dot{w}_{BLHT} - \dot{w}_{BLLT} - \dot{w}_{TPBL} - \dot{w}_3)dt + W_{3,i} \tag{B53}$$

$$T_3 = \frac{1}{\tau_3} \int_0^t (T_{3'} - T_3)dt + T_{3,i} \tag{B54}$$

$$P_3 = \frac{R_A W_3 T_3}{V_3} \tag{B55}$$

$$W_4 = \int_0^t (\dot{w}_3 + \dot{w}_{F,4} - \dot{w}_4)dt + W_{4,i} \tag{B56}$$

$$(WT)_4 = \gamma_4 \int_0^t \left[(\dot{w}T)_{4'} - \dot{w}_4 T_4\right]dt + (WT)_{4,i} \tag{B57}$$

$$T_4 = \frac{(WT)_4}{W_4} \tag{B58}$$

$$P_4 = \frac{R_A (WT)_4}{V_4} \tag{B59}$$

$$W_{4.1} = \int_0^t (\dot{w}_4 + \dot{w}_{BLHT} - \dot{w}_{4.1})dt + W_{4.1,i} \tag{B60}$$

$$(WT)_{4.1} = \gamma_{4.1} \int_0^t \left[(\dot{w}T)_{4.1'} - \dot{w}_{4.1} T_{4.1}\right]dt + (WT)_{4.1,i} \tag{B61}$$

$$T_{4.1} = \frac{(WT)_{4.1}}{W_{4.1}} \tag{B62}$$

$$P_{4.1} = \frac{R_A(WT)_{4.1}}{V_{4.1}} \tag{B63}$$

$$W_{13} = \int_0^t (\dot{w}_2 - \dot{w}_{2.2} - \dot{w}_{13})dt + W_{13,i} \tag{B64}$$

$$T_{13} = \frac{1}{\tau_{13}} \int_0^t (T_{13}' - T_{13})dt + T_{13,i} \tag{B65}$$

$$P_{13} = \frac{R_A W_{13} T_{13}}{V_{13}} \tag{B66}$$

$$W_6 = \int_0^t (\dot{w}_{13} + \dot{w}_{4.1} + \dot{w}_{BLLT} + \dot{w}_{TPBL} - \dot{w}_6)dt + W_{6,i} \tag{B67}$$

$$(WT)_6 = \gamma_6 \int_0^t \left[(\dot{w}T)_6' - \dot{w}_6 T_6\right]dt + (WT)_{6,i} \tag{B68}$$

$$T_6 = \frac{(WT)_6}{W_6} \tag{B69}$$

$$P_6 = \frac{R_A(WT)_6}{V_6} \tag{B70}$$

$$W_7 = \int_0^t (\dot{w}_6 + \dot{w}_{F,7} - \dot{w}_7)dt + W_{7,i} \tag{B71}$$

$$(WT)_7 = \gamma_7 \int_0^t \left[(\dot{w}T)_7' - \dot{w}_7 T_7\right]dt + (WT)_{7,i} \tag{B72}$$

$$T_7 = \frac{(WT)_7}{W_7} \tag{B73}$$

$$P_7 = \frac{R_A(WT)_7}{V_7} \tag{B74}$$

$$\dot{w}_{13} = \left(\frac{Ag_c}{l}\right)_D \int_0^t (P_{16'} - P_{16})dt + \dot{w}_{13,i} \tag{B75}$$

$$\dot{w}_6 = \left(\frac{Ag_c}{l}\right)_{AB} \int_0^t (P_{7'} - P_7)dt + \dot{w}_{6,i} \tag{B76}$$

$$(NQ)_{HT} = \frac{30J}{\pi} (\Delta h)_{HT}(\dot{w}_4 + K_{BLWHT}\dot{w}_{BLHT}) \tag{B77}$$

$$(NQ)_C = \frac{30J}{\pi} c_{p,2.2}\dot{w}_{2.2}\left(\frac{c_{p,3'}}{c_{p,2.2}} T_{3'} - T_2\right) \tag{B78}$$

$$\frac{c_{p,3'}}{c_{p,2.2}} = 0.9440^* + 0.00011385\ T_3 \tag{B79}$$

$$N_H = \frac{30}{\pi I_H} \int_0^t \left[\frac{(NQ)_{HT} - (NQ)_C}{N_H}\right] dt + N_{H,i} \tag{B80}$$

$$(NQ)_{LT} = \frac{30J}{\pi} (\Delta h)_{LT}(\dot{w}_{4.1} + K_{BLWLT}\dot{w}_{BLLT}) \tag{B81}$$

$$(NQ)_{FAN,OD} = \frac{30J}{\pi} c_{p,2}(\dot{w}_2 - \dot{w}_{2.2})\left(\frac{c_{p,1.3'}}{c_{p,2}} T_{1.3'} - T_2\right) \tag{B82}$$

*Adjusted for each flight condition to match rotor speeds at military power setting.

$$(NQ)_{FAN,ID} = \frac{30J}{\pi} c_{p,2} \dot{w}_{2.2} \left(\frac{c_{p,2.2}}{c_{p,2}} T_{2.2} - T_2 \right) \tag{B83}$$

$$\frac{c_{p,2.2}}{c_{p,2}} = 1.01^* \tag{B84}$$

$$N_L = \frac{30}{\pi I_L} \int_0^t \left[\frac{(NQ)_{LT} - (NQ)_{FAN,OD} - (NQ)_{FAN,ID}}{N_L} \right] dt + N_{L,i} \tag{B85}$$

*Adjusted for each flight condition to match rotor speeds at military power setting.

APPENDIX C

DIGITAL PROGRAM

FORTRAN Listing

```
      DIMENSION VALS(248),ZSC(2),PADR(3),PVAL(3),IDFORM(4)
C*****ADC VARIABLES FOR MAIN LOOP
      SCALED FRACTION X0,X1,X2,X3,X4,X5,X6,X7,X8,X9,X10,X11
      SCALED FRACTION X12,X13,X14,X15,X16,X17,X18
C*****ADC VARIABLES FOR OUTPUT LISTING
      SCALED FRACTION X19,X20,X21
C*****DAC VARIABLES
      SCALED FRACTION Y2,Y3,Y4,Y5,Y6,Y7,Y8,Y9,Y10,Y11,Y12
C*****OTHER VARIABLES
      SCALED FRACTION XVALS(10,8,6),YVALS(8,6),ZVALS(10,8,12),YI(24),
     1V9,V10,SSQRT,MAP2,MAP2L,V1,V2,V3,V4,V5,AR,PRSUB,DPR,PE,
     2PRE,PRSUP,FRD,V6,V7,V8,RT4,RT41
      COMMON/MAPS/XVALS,YVALS,ZVALS,IX(6),JY(6),NX(6),NY(6),
     1KX(6),KY(6)
      LOGICAL SENSW
      REAL M0
C*****INPUT REAL COMPONENT DATA AND MAP SCALE FACTORS
      TYPE 1
      TYPE 101
    1 FORMAT(/3X,33HPLACE DATA CARDS FOR MAPS NO. 2-9)
  101 FORMAT(3X,34HAND DAC ICS IN READER. THEN R-S-R./)
      PAUSE
C*****READ COMPRESSOR SVA AND COMPRESSOR P/P MAPS
      DO 5 N=2,3
      READ(6,4)(IDFORM(I),I=1,4),NCV,NPT
      READ(6,2)XSC,YSC,ZSC(1)
    2 FORMAT(4F8.2)
      NTBL=NCV*(2*NPT+1)
      READ(6,3)(VALS(I),I=1,NCV)
    3 FORMAT(8F8.4)
    4 FORMAT(4A2,2I3)
      J=NCV+1
      READ(6,IDFORM)(VALS(I),I=J,NTBL)
C*****SCALE MAPS 2-3
      DO 5 J=1,NCV
      YVALS(J,N)=VALS(J)/YSC
      DO 5 I=1,NPT
      JX=NCV+2*(J-1)*NPT+I
      XVALS(I,J,N)=VALS(JX)/XSC
      JZ1=JX+NPT
      ZVALS(I,J,N)=VALS(JZ1)/ZSC(1)
      IX(N)=1
      JY(N)=1
      NX(N)=NPT
      NY(N)=NCV
      KX(N)=0
      KY(N)=0
    5 CONTINUE
C*****READ FAN,HIGH TURBINE AND LOW TURBINE MAP DATA
      DO 7 N=4,6
```

```
      READ(6,4)(IDFORM(I),I=1,4),NCV,NPT
      READ(6,2)XSC,YSC,ZSC(1),ZSC(2)
      READ(6,3)(VALS(I),I=1,NCV)
      NTBL=NCV*(3*NPT+1)
      J=NCV+1
      READ(6,IDFORM)(VALS(I),I=J,NTBL)
C*****SCALE MAPS 4-9
  501 DO 6 J=1,NCV
      YVALS(J,N)=VALS(J)/YSC
      DO 6 I=1,NPT
      JX=NCV+3*(J-1)*NPT+I
      XVALS(I,J,N)=VALS(JX)/XSC
      JZ1=JX+NPT
      ZVALS(I,J,N)=VALS(JZ1)/ZSC(1)
      JZ2=JZ1+NPT
      N2=N+3
      ZVALS(I,J,N2)=VALS(JZ2)/ZSC(2)
    6 CONTINUE
      IX(N)=1
      JY(N)=1
      NX(N)=NPT
      NY(N)=NCV
      KX(N)=0
      KY(N)=0
    7 CONTINUE
C*****INITIALIZE DACS
      READ(6,9) (YI(I),I=1,24)
    9 FORMAT ((5(5X,S7)))
C*****INITIALIZE ANALOG CONSOLE
      CALL QSHYIN(IERR,680,680)
      CALL QSRUN(IERR)
      CALL QSMSN(IERR)
      CALL QSC(0,IERR)
      CALL QSC(1,IERR)
      DO 10  M=1,24
      MM=5*M-1
      CALL QWFRL(MM,.FALSE.,IERR)
   10 CONTINUE
C*****SPECIFY FLIGHT CONDITION FOR ENGINE
C*****TRANSFER INITIAL DAC VALUES
  105 CALL QWBDAS(YI,0,24,IERR)
      CALL QSTDA
      TYPE 11
      TYPE 111
   11 FORMAT(/3X,33HTYPE DESIRED VALUES FOR P0,T0,M0.)
  111 FORMAT(3X;33HDEPRESS SSW(D) FOR NO INLET LOSS./)
      ACCEPT 12,P0,T0,M0
   12 FORMAT(F7.3,F8.3,F5.2)
      T2Q0= (1.+.2*M0*M0)
      P2Q0= T2Q0**3.5
```

```
      ETAI= 1.0
      IF(SENSW(4))  GO TO 13
      IF(M0.LE.1.) GO TO 13
      ETAI= 1.0 - .075*(M0-1.)**1.35
   13 T2 = T2Q0*T0
      P2= P2Q0*P0 * ETAI
      P0SI= P0*.68948
      T0SI= T0*.55555
      P2SI= P2*.68948
      T2SI= T2*.55555
      TYPE 14,P2,T2
   14 FORMAT(/3X,5HP2 = ,F7.3,6H T2 = ,F8.3/)
      V1 = P2/40.
      V2 = T2/1000.
      V3= P0/20.
      V5=M0/3.
      V6=T0/1000.
      V5=V5*SSQRT(V6)
C*****PLACE ANALOG IN IC MODE
      TYPE 20
      TYPE 201
   20 FORMAT(/3X,36HSLAVE CONSOLES 2 AND 3 TO CONSOLE 1.)
  201 FORMAT(3X,18HMANUALLY GO TO IC.)
      TYPE 21
   21 FORMAT(3X,44HPROCEED TO DYNAMIC PART OF PROGRAM BY R-S-R./)
      PAUSE
C*****READ ADC VALUES AND GENERATE MAP OUTPUTS
   22 CALL QRBADS(X0,0,19,IERR)
      Y7=MAP2(4,X0,X1)
      IF(X8.GT..00000S)  GO TO 221
      Y7=Y7*(.99999S+.06633S*X8)
  221 Y5=MAP2L(7)
      IF(X9.GT..00000S)  X9=.00000S
      V4=MAP2(2,X3,-X9)
      Y6=MAP2(3,X2,X3)
      Y6=(.50100S*Y6)/(.50000S*V4+.50000S)
      RT4=SSQRT(X17)
      V7=.86138S*X5/RT4
      Y8=MAP2(5,X4,V7)
      V9=MAP2L(8)
      RT41=SSQRT(X18)
      V8=.84864S*X7/RT41
      Y10=MAP2(6,X6,V8)
      V10=MAP2L(9)
      Y9=-V9*RT4/.84895S
      Y11=-V10*RT41/.50000S
      Y2=Y6
      Y3=Y7
      Y4=X10*X11
      Y5=Y5/.99800S
```

```
      AR=X12/.97838S-.61418S*X12*X12+.26876S
      DPR=(.69683S*AR*AR-AR+.32894S)/.18567S
      PRSUB=.52828S-DPR
      PE=PRSUB*X13
      FRD=.58481S*X16*V5
      IF(.33333S*V3.LT.PE)  GO TO 225
      PRE=.33333S*V3/X13
      Y12=(X15*SSQRT((.2578S-.2578S*PRE)*X14)-FRD)/.34933S
      GO TO 23
  225 PRSUP=.52828S+DPR
      PE=PRSUP*X13/.66667S
      Y12=(X15*SSQRT((.47383S-PRSUP/.98186S+.85865S*PRSUP*PRSUP)
     1 *X14)-FRD-.93154S*X12*AR*(.58888S*V3-PE))/.34933S
C*****TRANSFER UPDATED DAC VALUES TO ANALOG
   23 CALL QWBDAS(Y2,2,11,IERR)
      CALL QSTDA
C*****OUTPUT UNSCALED DATA AT TELETYPE IF DESIRED
      IF(.NOT.SENSW(1))  GO TO 22
      CALL QRBADS(X19,19,3,IERR)
      P13Q2 = X8
      P13Q2 = P13Q2*1.5*3.8816
      XNLR2= X1
      XNLR2=XNLR2*1.2*9872.8
      P3Q22=X2
      P3Q22= P3Q22*1.5*8.4621
      XNHR22 = X3
      XNHR22=XNHR22*1.1*9942.3
      P41Q4=X4
      P41Q4=P41Q4*3.8*.25784
      CNHPT = V7
      CNHPT=CNHPT*1.25*2288.28
      CNHTSI =CNHPT*1.3416
      P5Q41=X6
      P5Q41=P5Q41*2.8*.47763
      CNLPT = V8
      CNLPT=CNLPT*1.5*215.14
      CNLTSI= CNLPT*1.3416
      GVIPOS=X8
      GVIPOS=GVIPOS*25.-     5.4
      HVSPOS=X9
      HVSPOS=HVSPOS*48.+2.5
      WF4=X18
      WF4 = WF4*4.
      WF4SI= WF4*.45359
      WF4=WF4*3688.
      AN=X12
      AN = AN*1888.
      ANSI = AN*.88864516
      AN=AN/144.
      P4=X21
```

```
      P4 = P4*500.
      P4SI = P4*.68948
      XNL=X7
      XNL= XNL*15000.
      XNH=X5
      XNH= XNH*15000.
      T4=X17
      T4= T4*4000.
      T4SI= T4*.55555
      PLA = X19
      PLA= PLA*150.
      T7=X14
      T7 = T7*5000.
      T7SI= T7*.55555
      WF7 = X20
      WF7 = WF7*20.
      WF7SI= WF7*.45359
      WF7=WF7*3600.
      WA2=X16
      WA2= WA2*300.
      WA2SI= WA2*.45359
      T41=X18
      T41=T41*3000.
      T41SI=T41*.55555
      P21Q2= Y5
      P21Q2=P21Q2*1.5*2.9931
      WAR22= Y6
      WAR22=WAR22*1.1*54.988
      WR22SI= WAR22*.45359
      WAR2 = Y7
      WAR2=WAR2*1.2*221.57*1.007
      WAR2SI= WAR2*.45359
      WPHPT= Y8
      WPHPT=WPHPT*1.30*.68257
      WPHTSI= WPHPT*.36548
      HPHPT = V9
      HPHPT=HPHPT*1.25*.31043
      HPHTSI= HPHPT*3118.7
      WPLPT= Y10
      WPLPT=WPLPT*2.5*.31761
      WPLTSI= WPLPT*.36548
      HPLPT = V10
      HPLPT=HPLPT*2.5*.19522
      HPLTSI= HPLPT*3118.7
      FN=Y12
      FN=FN*30000.
      FNSI=FN*4.4482E-3
      TYPE 24
   24 FORMAT(21X,33HF100 SIMULATION STEADY-STATE DATA//)
      IF(.NOT.SENSW(2)) GO TO 441
```

```
   TYPE 25,P0SI,P0
25 FORMAT(5X,9HP0      = ,F7.3,9X,7HN/SQ CM,7X,2H( ,F7.3,9X,8HPSIA    )
  1)
   TYPE 26,T0SI,T0
26 FORMAT(5X,9HT0      = ,F7.2,9X,7HK       ,7X,2H( ,F7.2,9X,8HR      )
  1)
   TYPE 27,M0
27 FORMAT(5X,9HM0      = ,F7.4)
   TYPE 28,P2SI,P2
28 FORMAT(5X,9HP2      = ,F7.3,9X,7HN/SQ CM,7X,2H( ,F7.3,9X,8HPSIA    )
  1)
   TYPE 29,T2SI,T2
29 FORMAT(5X,9HT2      = ,F7.2,9X,7HK       ,7X,2H( ,F7.2,9X,8HR      )
  1)
   TYPE 30,PLA
30 FORMAT(5X,9HPLA     = ,F7.2,9X,3HDEG)
   TYPE 31,WF4SI,WF4
31 FORMAT(5X,9HWF4     = ,F7.4,9X,7HKG/SEC ,7X,2H( ,F7.0,9X,8HLBM/HR )
  1)
   TYPE 32,WF7SI,WF7
32 FORMAT(5X,9HWF7     = ,F7.3,9X,7HKG/SEC ,7X,2H( ,F7.0,9X,8HLBM/HR )
  1)
   TYPE 33,GVIPOS
33 FORMAT(5X,9HGVIPOS  = ,F7.3,9X,3HDEG)
   TYPE 34,HVSPOS
34 FORMAT(5X,9HHVSPOS  = ,F7.3,9X,3HDEG)
   TYPE 35,ANSI,AN
35 FORMAT(5X,9HAN      = ,F7.5,9X,7HSQ M    ,7X,2H( ,F7.4,9X,8HSQ FT   )
  1)
   TYPE 36,XNH
36 FORMAT(5X,9HXNH     = ,F7.0,9X,3HRPM)
   TYPE 37,XNL
37 FORMAT(5X,9HXNL     = ,F7.0,9X,3HRPM)
   TYPE 38,WA2SI,WA2
38 FORMAT(5X,9HWA2     = ,F7.2,9X,7HKG/SEC ,7X,2H( ,F7.2,9X,8HLBM/SEC)
  1)
   TYPE 40,P4SI,P4
40 FORMAT(5X,9HP4      = ,F7.2,9X,7HN/SQ CM,7X,2H( ,F7.2,9X,8HPSIA    ).
  1)
```

```
      TYPE 41,FNSI,FN
   41 FORMAT(5X,9HFN      = ,F7.2,9X,7HKN      ,7X,2H( ,F7.0,9X,8HLBF     )
     1)
      TYPE 42,T4SI,T4
   42 FORMAT(5X,9HT4      = ,F7.1,9X,7HK       ,7X,2H( ,F7.1,9X,8HR       )
     1)
      TYPE 39,T41SI,T41
   39 FORMAT(5X,9HT41     = ,F7.1,9X,7HK       ,7X,2H( ,F7.1,9X,8HR       )
     1)
      TYPE 43,T7SI,T7
   43 FORMAT(5X,9HT7      = ,F7.1,9X,7HK       ,7X,2H( ,F7.1,9X,8HR       )
     1)
      TYPE 45,P13Q2
      IF(.NOT.SENSW(3))  GO TO 22
   45 FORMAT(5X,9HP13Q2   = ,F7.4)
  441 TYPE 46,XNLR2
   46 FORMAT(5X,9HXNLR2   = ,F7.0,9X,3HRPM)
      TYPE 47,WAR2SI,WAR2
   47 FORMAT(5X,9HWAR2    = ,F7.2,9X,7HKG/SEC ,7X,2H( ,F7.2,9X,8HLBM/SEC)
     1)
      TYPE 48,P21Q2
   48 FORMAT(5X,9HP21Q2   = ,F7.4)
      TYPE 49,P3Q22
   49 FORMAT(5X,9HP3Q22   = ,F7.3)
      TYPE 50,XNHR22
   50 FORMAT(5X,9HXNHR22 = ,F7.0,9X,3HRPM)
      TYPE 51,WR22SI,WAR22
   51 FORMAT(5X,9HWAR22   = ,F7.2,9X,7HKG/SEC ,7X,2H( ,F7.2,9X,8HLBM/SEC)
     1)
      TYPE 52,P41Q4
   52 FORMAT(5X,9HP41Q4   = ,F7.5)
      TYPE 53,CNHTSI,CNHPT
   53 FORMAT(5X,9HCNHPT   = ,F7.2,9X,7H        ,7X,2H( ,F7.2,9X,8H        )
     1)
      TYPE 54,WPHTSI,WPHPT
   54 FORMAT(5X,9HWPHPT   = ,F7.5,9X,7H        ,7X,2H( ,F7.5,9X,8H        )
     1)
      TYPE 55,HPHTSI,HPHPT
   55 FORMAT(5X,9HHPHPT   = ,F7.1,9X,7H        ,7X,2H( ,F7.5,9X,8H        )
     1)
      TYPE 56,P5Q41
   56 FORMAT(5X,9HP5Q41   = ,F7.5)
      TYPE 57,CNLTSI,CNLPT
```

```
57 FORMAT(5X,9HCNLPT  = ,F7.2,9X,7H        ,7X,2H( ,F7.2,9X,8H        )
  1)
   TYPE 58,WPLTSI,WPLPT
58 FORMAT(5X,9HWPLPT  = ,F7.5,9X,7H        ,7X,2H( ,F7.5,9X,8H        )
  1)
   TYPE 59,HPLTSI,HPLPT
59 FORMAT(5X,9HHPLPT  = ,F7.1,9X,7H        ,7X,2H( ,F7.5,9X,8H        )
  1)
   GO TO 22
   END
```


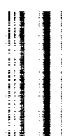

FORTRAN Symbols

AN	exhaust nozzle throat area, ft^2
ANSI	exhaust nozzle throat area, m^2
AR	exhaust nozzle expansion ratio (scaled)
CNHPT	high-pressure-turbine corrected speed, $rpm/{}^{o}R^{1/2}$
CNHTSI	high-pressure-turbine corrected speed, $rpm/K^{1/2}$
CNLPT	low-pressure-turbine corrected speed, $rpm/{}^{o}R^{1/2}$
CNLTSI	low-pressure-turbine corrected speed, $rpm/K^{1/2}$
DPR	shift in critical pressure ratio due to expansion ratio
ETAI	inlet efficiency
FN	net thrust (uninstalled), lbf
FNSI	net thrust (uninstalled), kN
FRD	ram drag (scaled)
GVIPOS	inlet guide vane position, deg
HPHPT	high-pressure-turbine enthalpy drop parameter, $Btu/lbm-{}^{o}R^{1/2}-rpm$
HPHTSI	high-pressure-turbine enthalpy drop parameter, $J/kg-K^{1/2}-rpm$
HPLPT	low-pressure-turbine enthalpy drop parameter, $Btu/lbm-{}^{o}R^{1/2}-rpm$
HPLTSI	low-pressure-turbine enthalpy drop parameter, $J/kg-K^{1/2}-rpm$
HVSPOS	stator vane position, deg
I	integer
IDFORM	array containing alphanumeric format data
IERR	error flag for linkage routines
IX	array containing number of points per curve for each map pair
J	integer
JX	map scaling index
JY	array containing number of curves for each map pair
JZ1	map scaling index
JZ2	map scaling index
KX	array containing x out-of-range counts for each map pair

KY	array containing y out-of-range counts for each map pair
MAP2	bivariate function (first function)
MAP2L	bivariate function (second function)
MM	function relay address
M0	Mach number
N	map index
NCV	number of curves for map being read in
NPT	number of points per curve for map being read in
NTBL	number of data points for map being read in
NX	array containing number of points per curve for each map pair
NY	array containing number of curves for each map pair
N2	integer
PADR	array containing potentiometer addresses
PE	exhaust plane pressure (scaled)
PLA	power lever angle, deg
PRE	nozzle pressure ratio
PRSUB	critical nozzle pressure ratio
PRSUP	design pressure ratio for supersonic nozzle flow
PVAL	array containing potentiometer settings
PI	pressure at station I, psia
PISI	pressure at station I, N/cm^2
PJQI	ratio of pressure at station J to pressure at station I
QRBADS	linkage routine for reading ADC's
QSC	linkage routine for selecting analog console
QSHYIN	linkage routine for addressing analog consoles
QSMSN	linkage routine for setting analog time scale to normal milliseconds (N-MS)
QSPC	linkage routine for selecting potentiometer coefficient mode
QSRUN	linkage routine for selecting logic run mode
QSTDA	linkage routine for transferring DAC data
QWBDAS	linkage routine for loading DAC's

QWFRL	linkage routine for positioning function relays
RT4	square root of T4 (scaled)
RT41	square root of T41 (scaled)
SENSW	array containing logical indication of sense switch positions
SSQRT	scaled-fraction square root routine
TI	temperature at station I, ^{o}R
TISI	temperature of station I, K
TJQI	ratio of temperature at station J to temperature at station I
VALS	array containing unscaled map data
V1	fan inlet pressure (scaled)
V2	fan inlet temperature (scaled)
V3	ambient pressure (scaled)
V4	shift in compressor map corrected airflow due to change in stator vane position (scaled)
V5	Mach number (scaled)
V6	ambient temperature (scaled)
V7	high-pressure-turbine corrected speed (scaled)
V8	low-pressure-turbine corrected speed (scaled)
V9	high-pressure-turbine enthalpy drop parameter (scaled)
V10	low-pressure-turbine enthalpy drop parameter (scaled)
WA2	fan airflow, lbm/sec
WA2SI	fan airflow, kg/sec
WAR2	fan corrected airflow, lbm/sec
WAR22	compressor corrected airflow, lbm/sec
WAR2SI	fan corrected airflow, kg/sec
WF4	main-combustor fuel flow, lbm/hr
WF4SI	main-combustor fuel flow, kg/hr
WF7	augmentor fuel flow, lbm/hr
WF7SI	augmentor fuel flow, kg/hr
WPHPT	high-pressure-turbine corrected flow, lbm-^{o}R-in.^{2}/lbf-rpm-sec

WPHTSI	high-pressure-turbine corrected flow, kg-K-cm^2/N-rpm-sec
WPLPT	low-pressure-turbine corrected flow, lbm-^oR-$in.^2$/lbf-rpm-sec
WPLTSI	low-pressure-turbine corrected flow, kg-K-cm^2/N-rpm-sec
WR22SI	compressor corrected airflow, kg/sec
XNH	high-speed-rotor speed, rpm
XNHR22	compressor corrected speed, rpm
XNL	low-speed-rotor speed, rpm
XNLR2	fan corrected speed, rpm
XSC	scale factor for map input x
XVALS	array containing scaled map input x data
XI	variable read on ADC channel I
YSC	scale factor for map input y
YVALS	array containing scaled map input y data
YI	variable output of DAC channel I
ZSC	array containing scale factor for map output z
ZVALS	array containing scaled map output z data

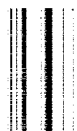

APPENDIX D

ANALOG PATCHING DIAGRAMS AND POTENTIOMETER SETTINGS

Analog Patching Diagrams

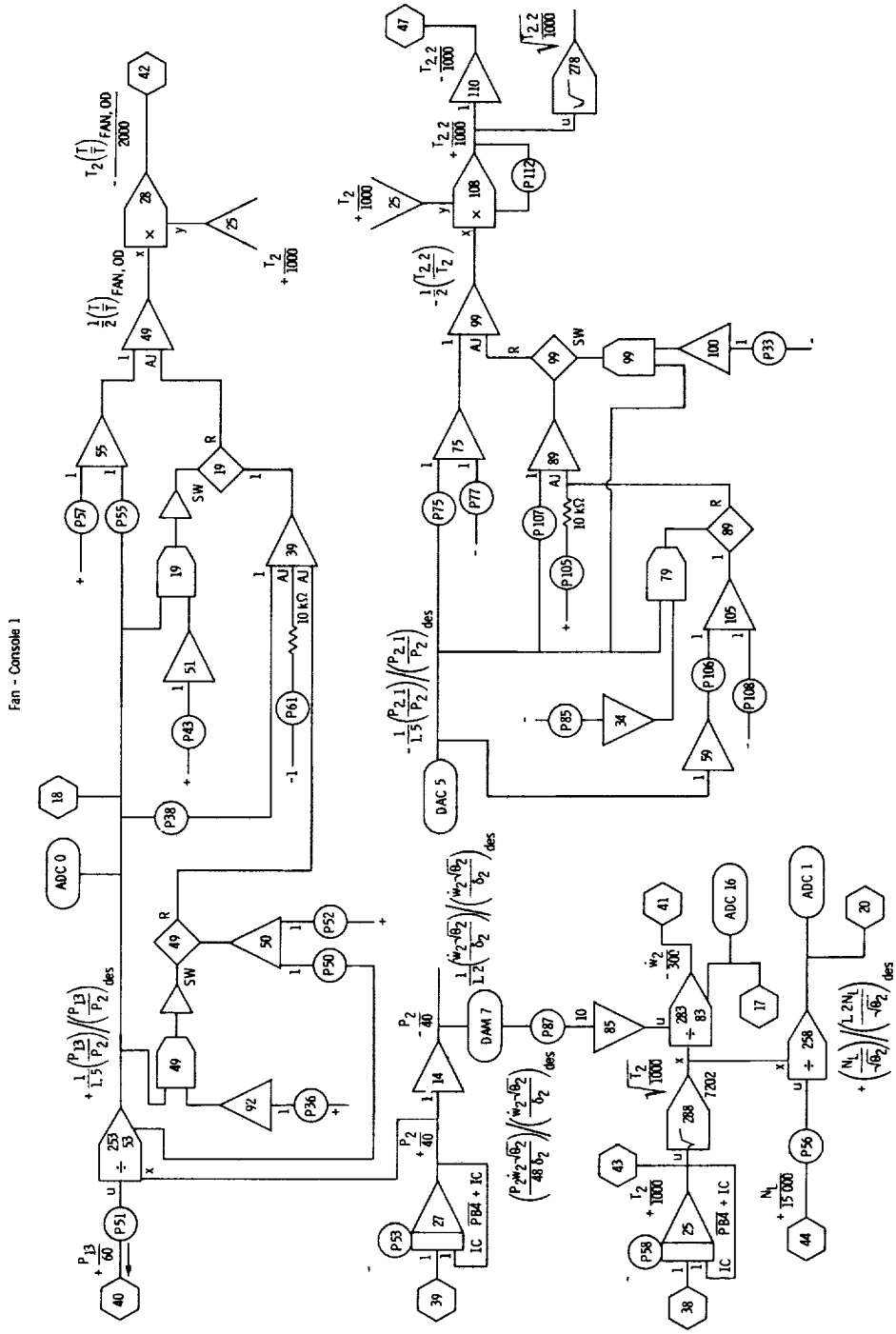

Compressor - Console 1

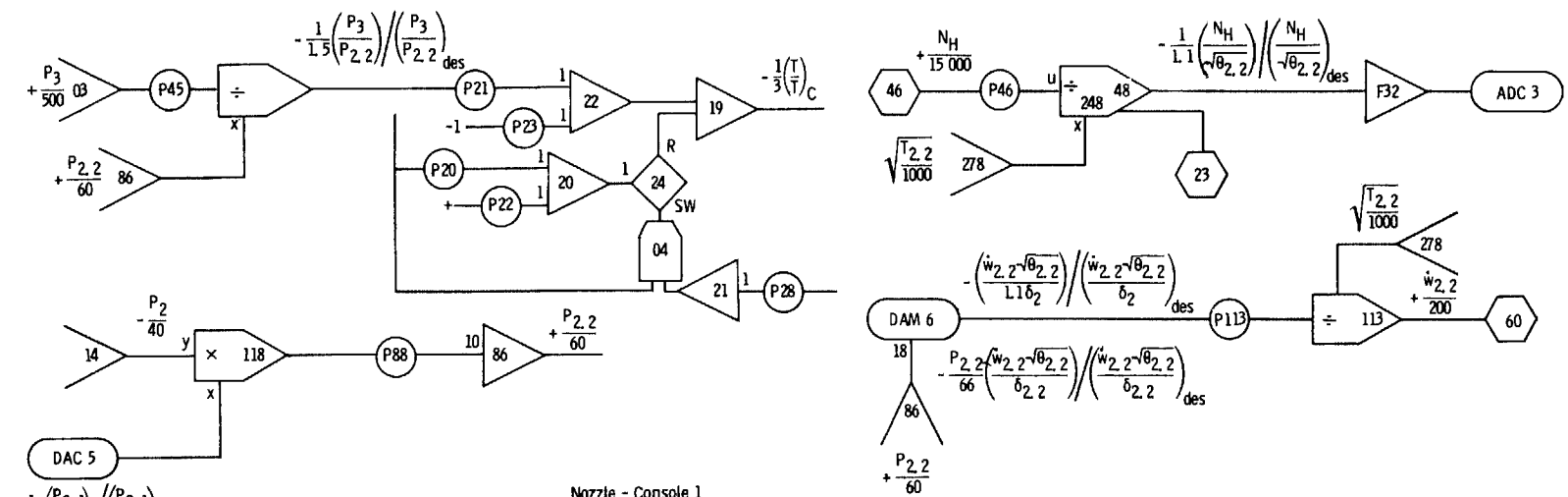

Nozzle - Console 1

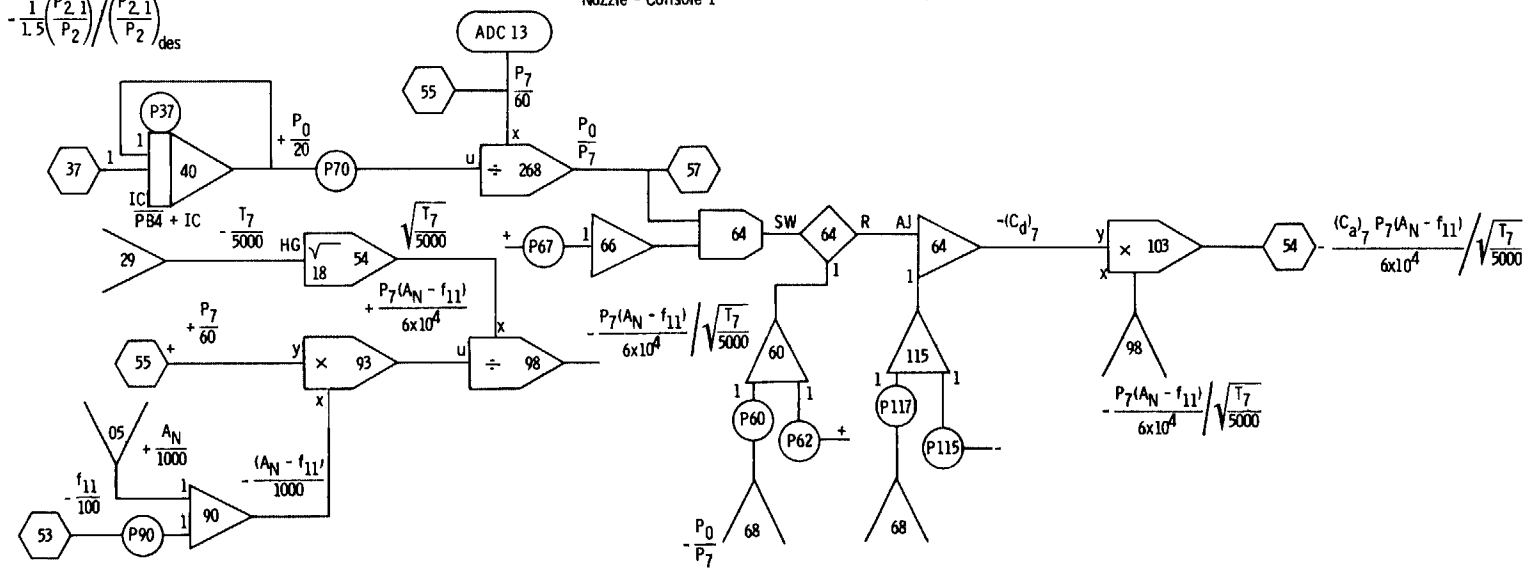

Main Combustor - Console 1

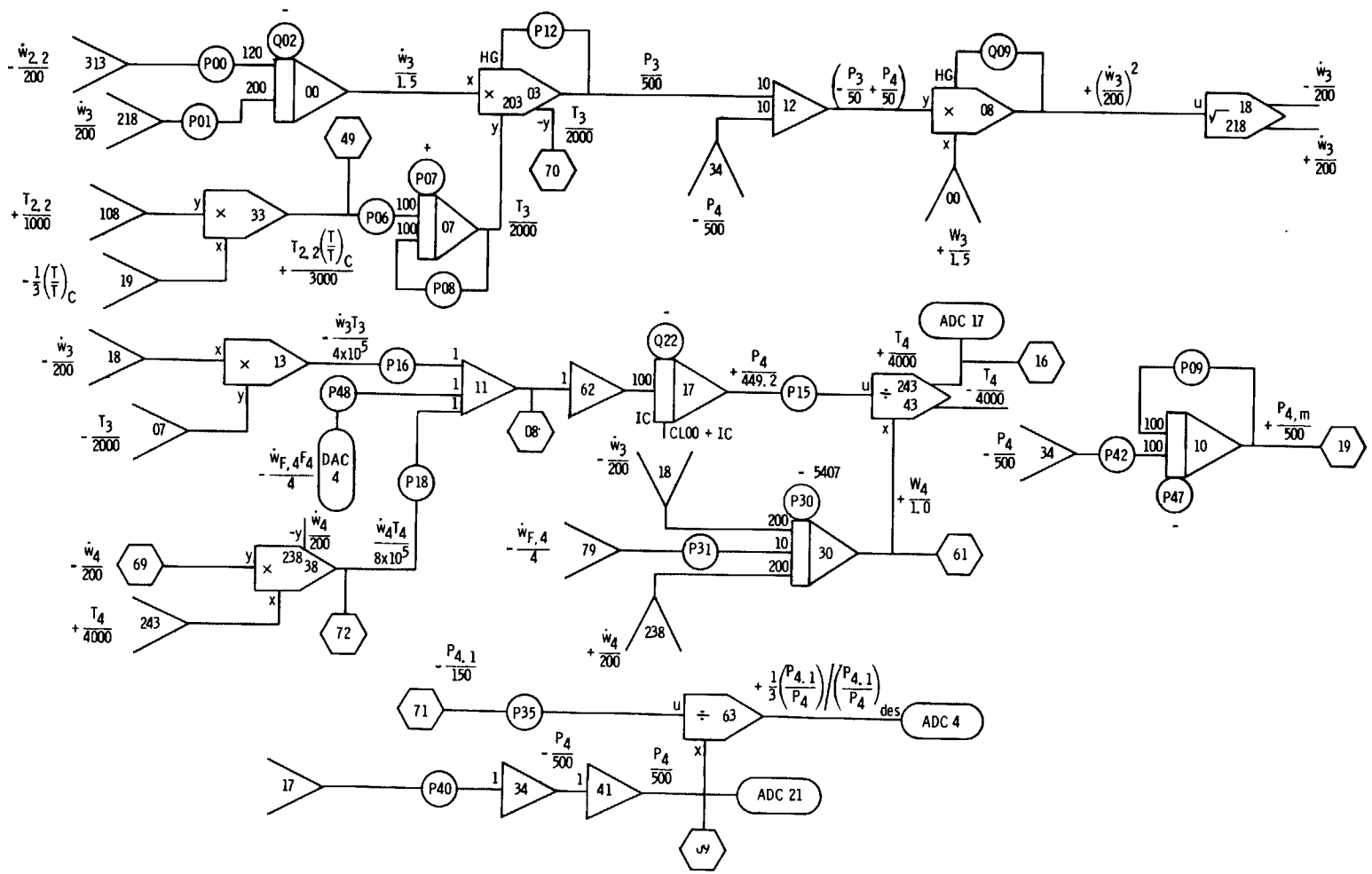

Hybrid Interface - Console 1

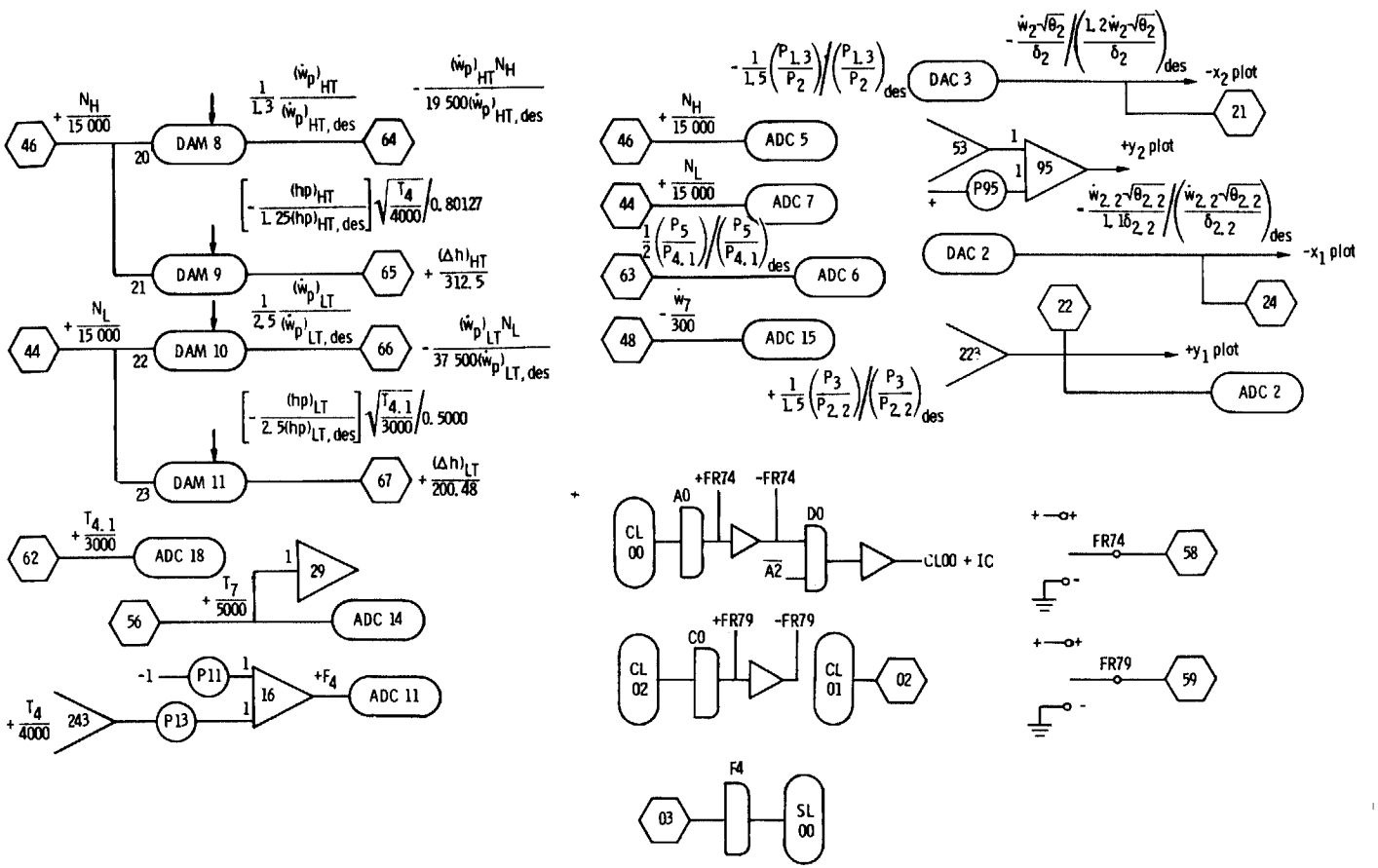

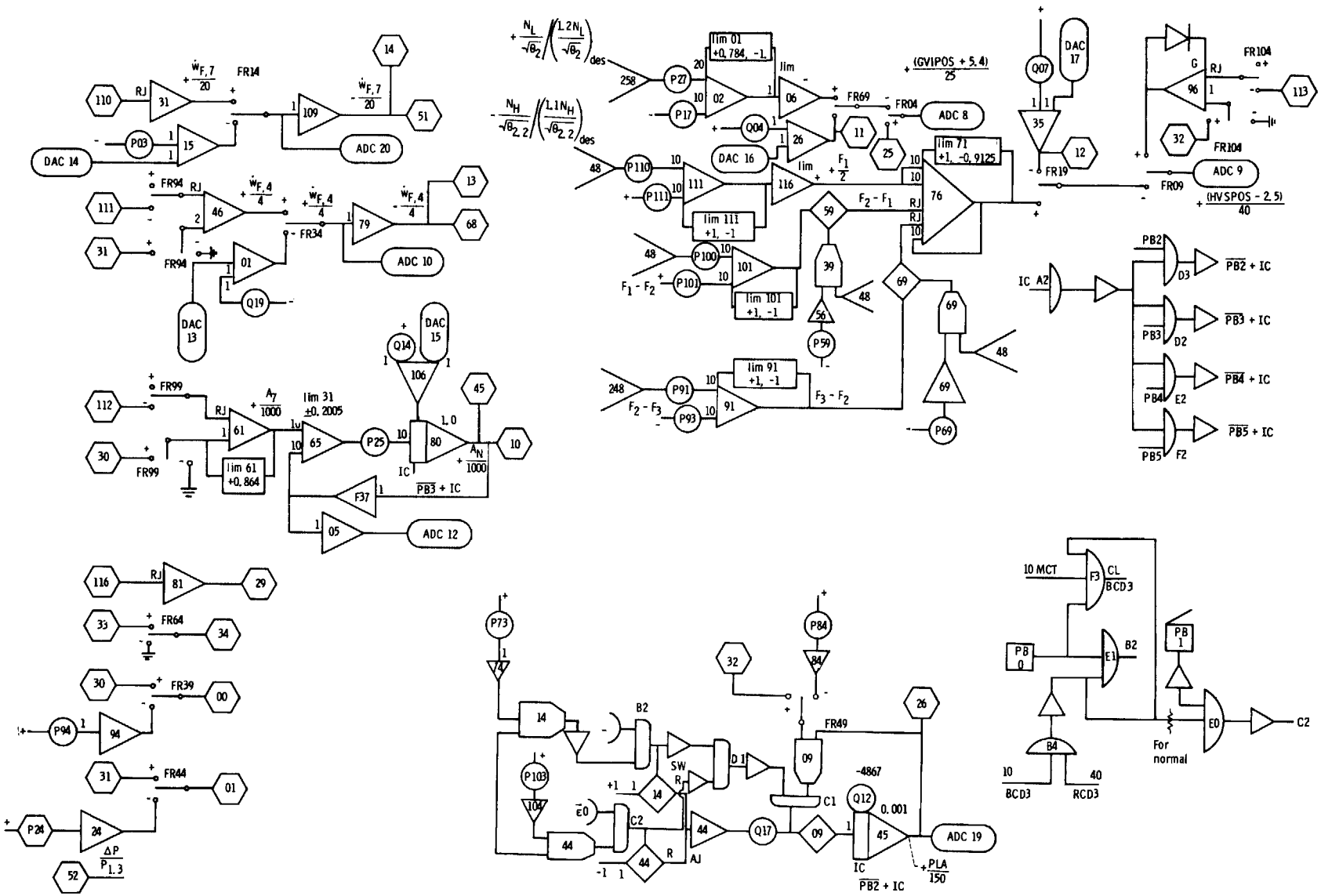
DAC 14
DAC 13
DAC 15
DAC 16
DAC 17
ADC 20
ADC 10
ADC 12
ADC 8
ADC 9
ADC 19
lim 01 +0.784, -1.
lim 71 +1, -0.9125
lim 31 ±0.2005
lim 61 +0.864
lim 111 +1, -1
lim 101 +1, -1
lim 91 +1, -1
FR14
FR34
FR94
FR99
FR64
FR39
FR44
FR69
FR04
FR49
FR19
FR09
FR104
(GVIPOS + 5.4)/25
(HVSPOS - 2.5)/40
F2 - F1
F1 - F2
F2 - F3
F3 - F2
PB2 D3
PB3 D2
PB4 E2
PB5 F2
IC A2
PB2 + IC
PB3 + IC
PB4 + IC
PB5 + IC
10 MCT
CL BCD3
For normal
10 BCD3
40 RCD3
-4867
0.001
+PLA/150

Fan Duct - Console 2

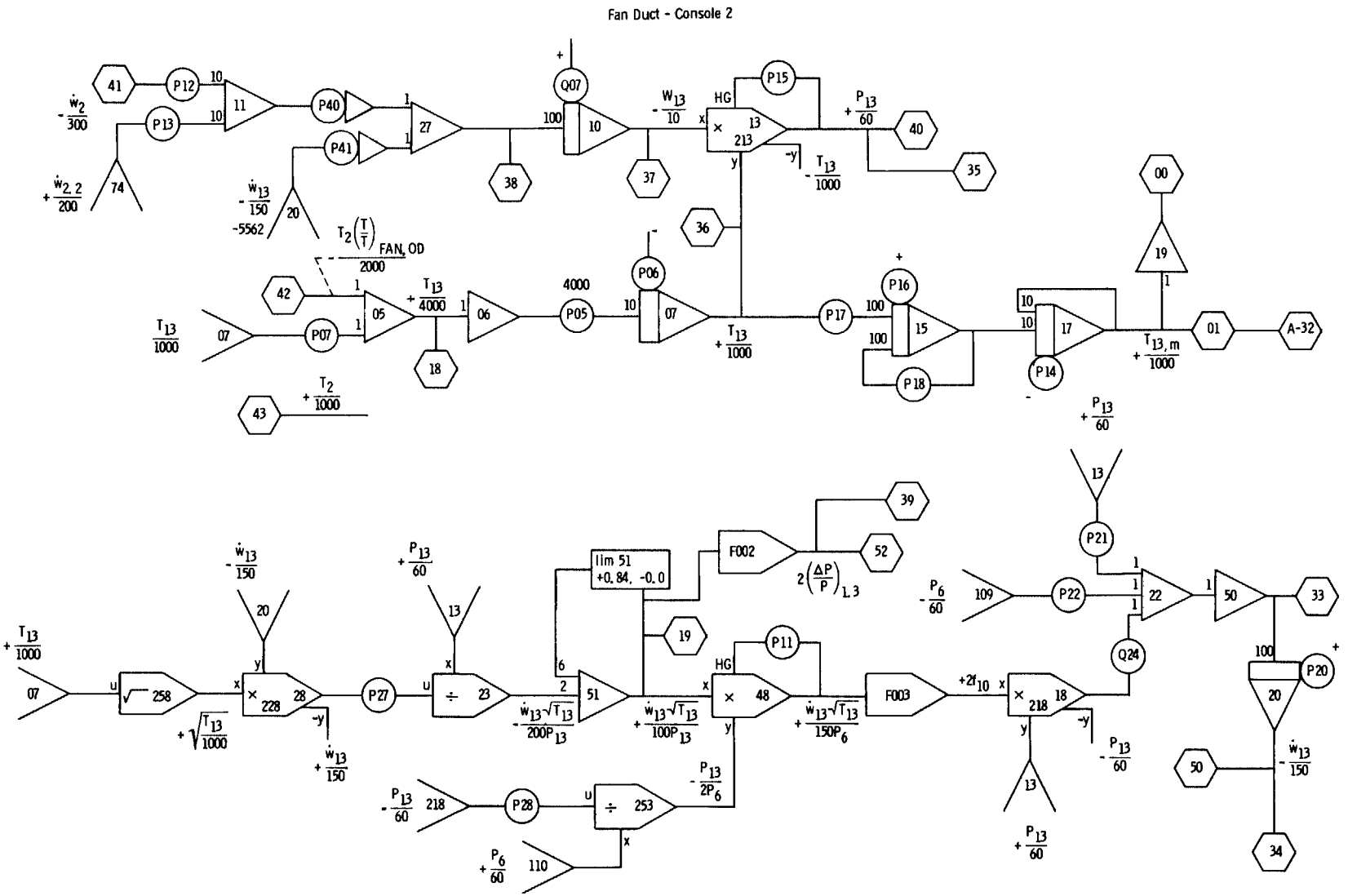

High-Pressure Turbine - Console 2

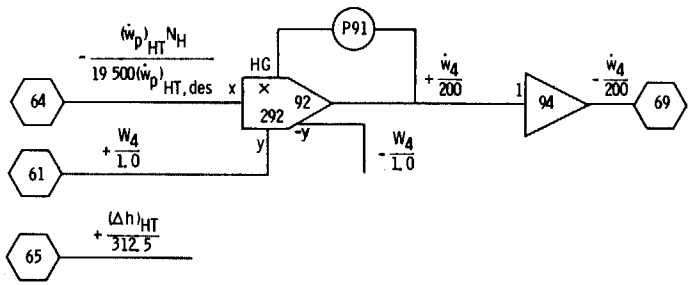

Low-Pressure Turbine - Console 2

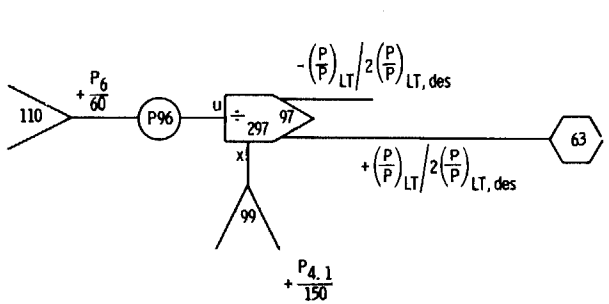

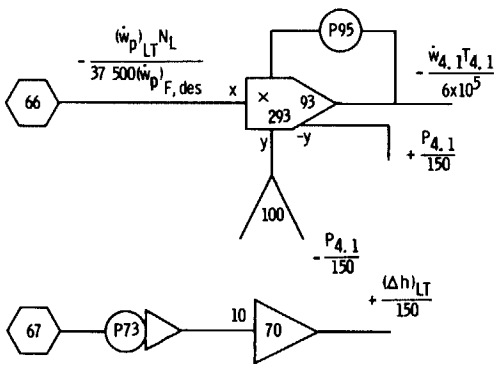

Interturbine Volume - Console 2

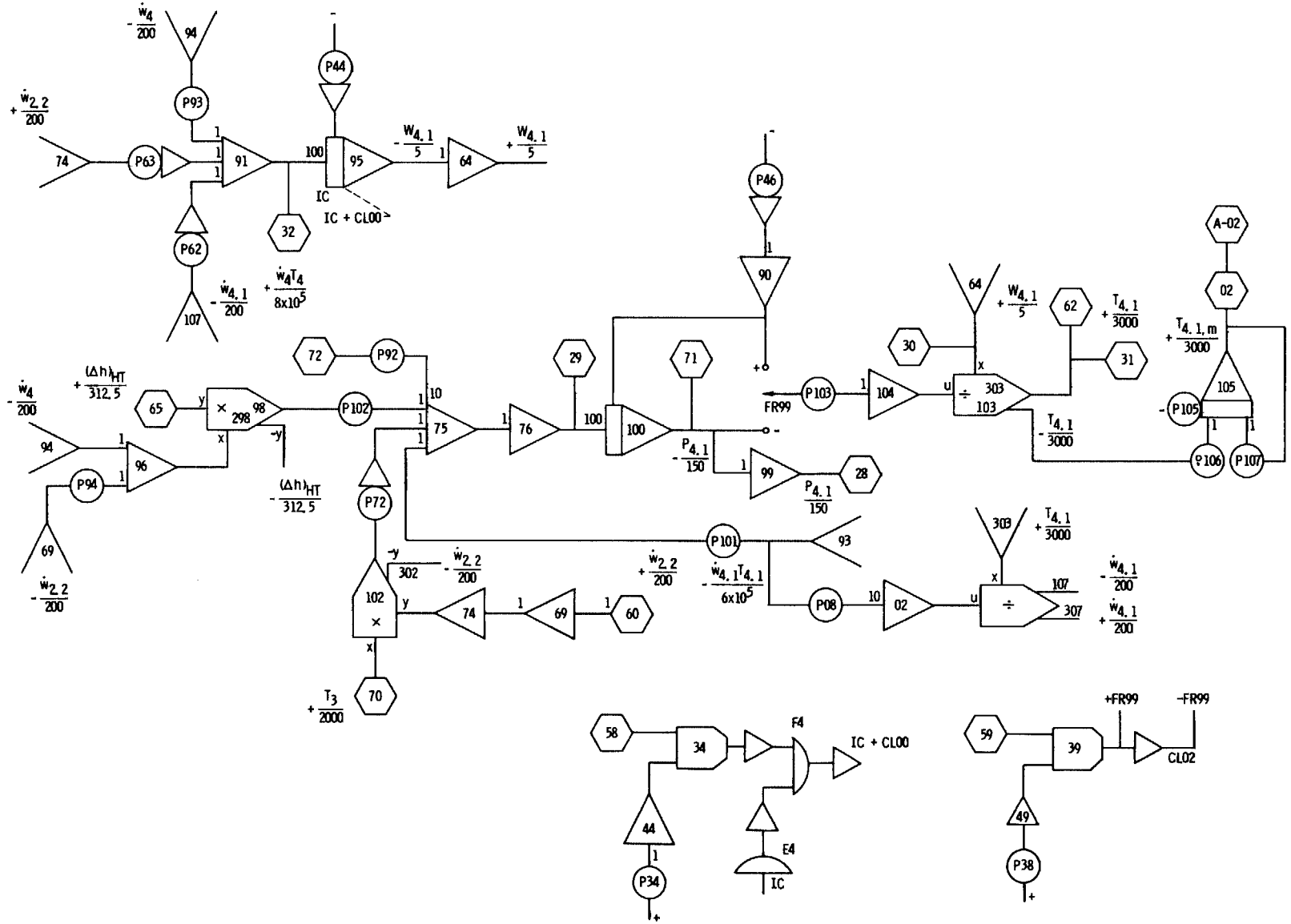

Mixing Volume - Console 2

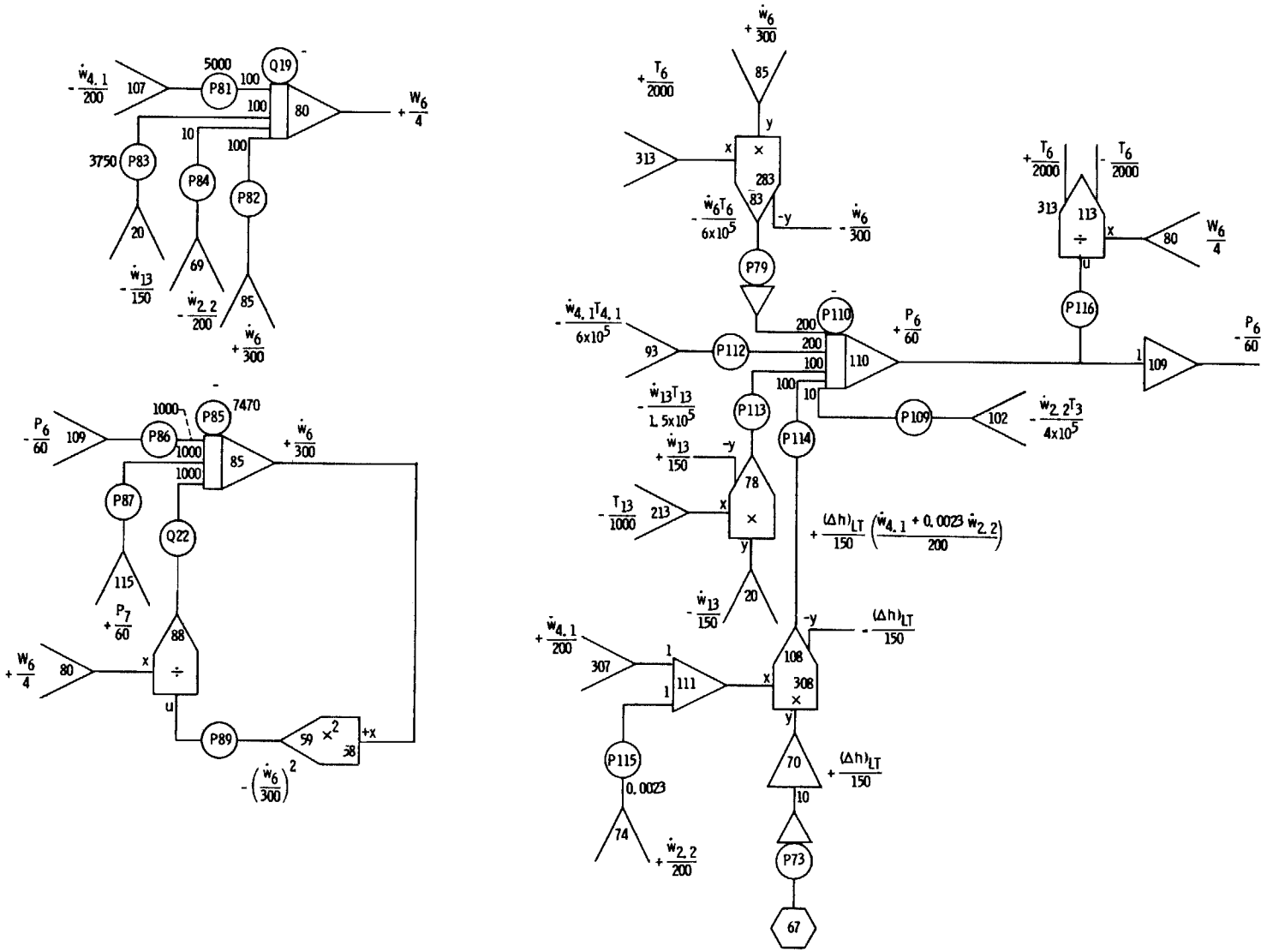

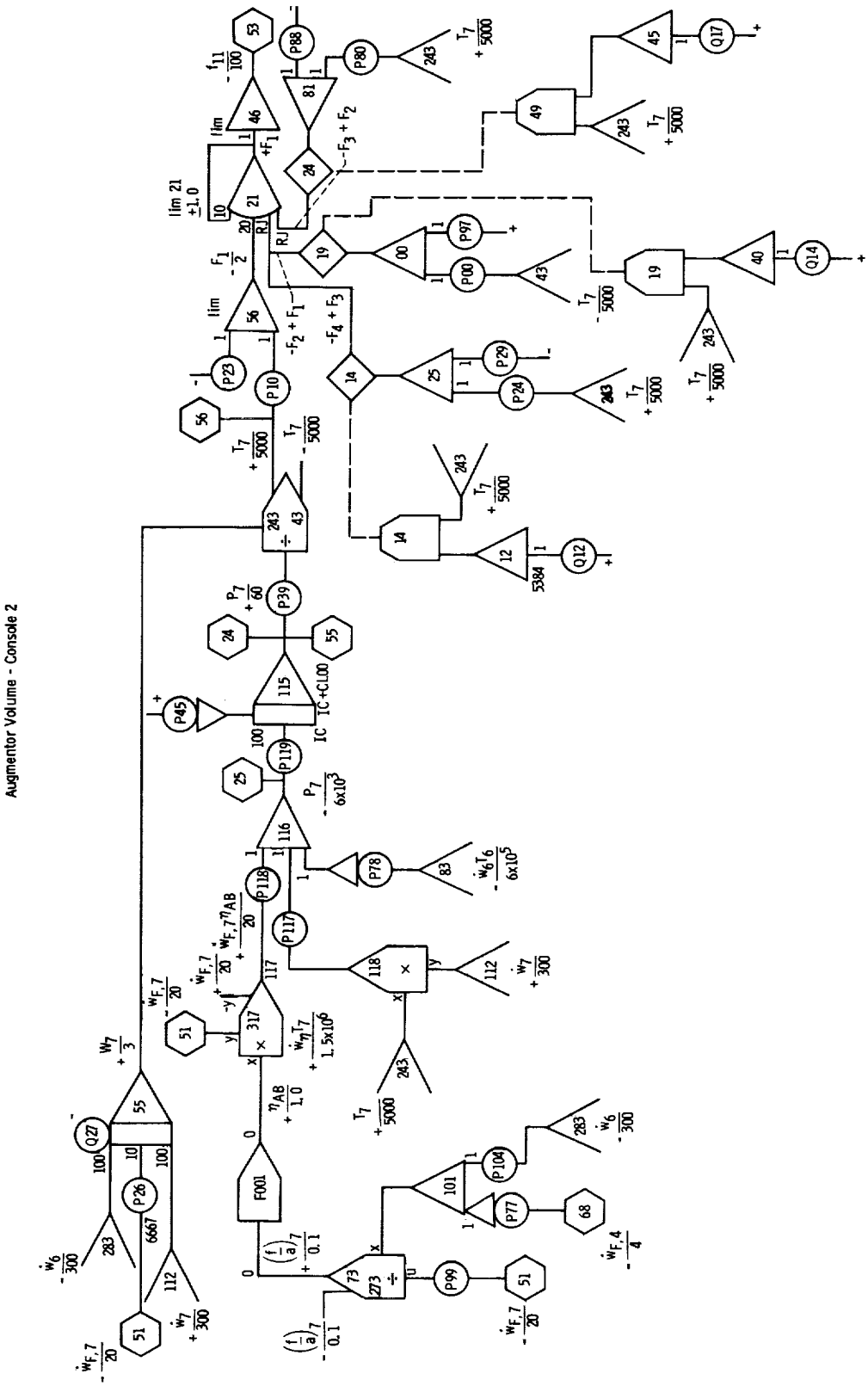
Augmentor Volume - Console 2

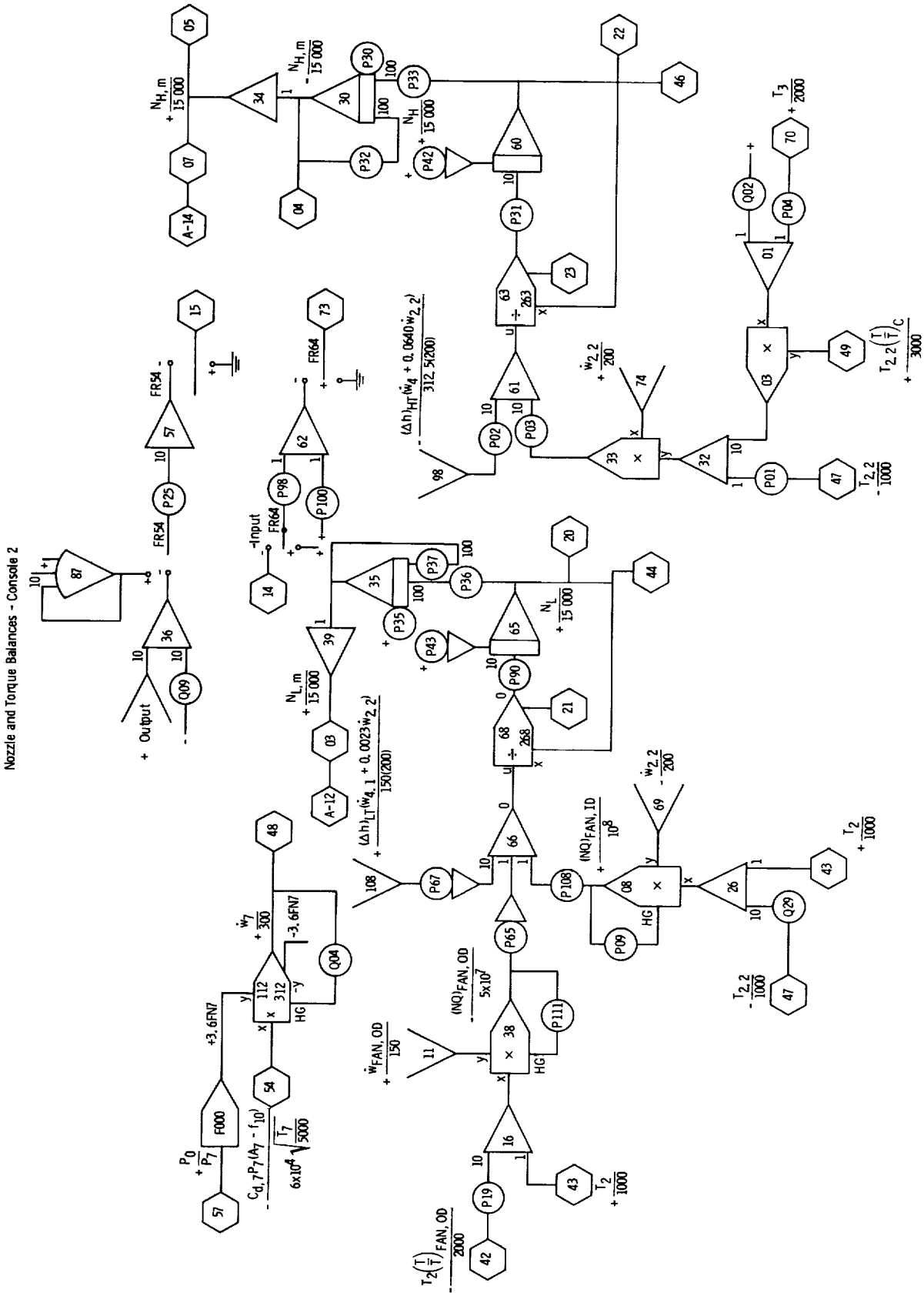
Nozzle and Torque Balances - Console 2
+ Output
-Input
FR54
FR64
$\frac{N_{H,m}}{15\,000}$
$\frac{N_H}{15\,000}$
$\frac{N_L}{15\,000}$
$\frac{N_{L,m}}{15\,000}$
$\frac{\dot{w}_7}{300}$
$\frac{\dot{w}_{2.2}}{200}$
$\frac{P_0}{P_7}$
$\frac{T_2}{1000}$
$\frac{T_{2.2}}{1000}$
$\frac{T_3}{2000}$
$\frac{T_{2.2}}{3000}$
$\frac{\dot{w}_{FAN,OD}}{150}$
$\frac{(NQ)_{FAN,OD}}{5\times10^7}$
$\frac{(NQ)_{FAN,ID}}{10^8}$
$\frac{T_2}{2000}$
-3.6FN7
+3.6FN7
$6\times10^4\sqrt{\frac{T_7}{5000}}$
$\frac{(\Delta h)_{LT}(\dot{w}_{4.1}+0.0023\dot{w}_{2.2})}{150(200)}$
$\frac{(\Delta h)_{HT}(\dot{w}_4+0.0640\dot{w}_{2.2})}{312.5(200)}$

F100-PW-100 Real-Time Simulation Potentiometer Settings

Used With 680 Analog Computer (Console 1)†

Potentiometer	Setting	Potentiometer	Setting	Potentiometer	Setting	Potentiometer	Setting
P00	0.9330	P30	0.5410	P58	0.5187	P101	0.3993
P01	.6667	P31	.4000	P59	.8241	P103	.1333
P03	.0001	P33	.4544	P60	.0768	P105	.0607
P06	.3006	P35	.3876	P61	.0648	P106	.1753
P07	.7274	P36	.3109	P62	.0384	P107	.1336
P08	.2000	P37	.7348	P67	.5000	P108	.0575
P09	.8333	P38	.1576	P69	.7642	P110	.2840
P11	.2388	P40	.8985	P70	.3333	P111	.2528
P12	.7430	P42	.8333	P73	.8467	P112	.4996
P13	.0785	P43	.4109	P75	.3608	P113	.8898
P15	.5000	P45	.6566	P77	.4699	P115	.9394
P16	.1215	P46	.9891	P84	.1333	P117	.0277
P17	.9010	P47	.7027	P85	.3296	Q02	.7603
P18	.2674	P48	.5001	P87	.1752	Q04	.0000
P20	.1339	P50	.1502	P88	.3001	Q07	.0000
P21	.2969	P51	.3336	P90	.1000	Q09	.9458
P22	.0606	P52	.0466	P91	.5780	Q12	.4867
P23	.4607	P53	.3674	P93	.4417	Q14	.4156
P24	.0712	P55	.4127	P94	.5011	Q17	.0767
P25	.3333	P56	.9132	P95	.2221	Q19	.6989
P27	.5442	P57	.4525	P100	.4845	Q22	.7823
P28	.4530						

†Scale factors and parameters are in engineering units (U.S. customary units).

F100-PW-100 Real-Time Simulation Potentiometer Settings

Used With 681 Analog Computer (Console 2)‡

Potentiometer	Setting	Potentiometer	Setting	Potentiometer	Setting	Potentiometer	Setting
P00	0.8150	P28	0.5000	P79	0.8550	P106	0.2000
P01	.6667	P29	.2511	P80	.4414	P107	.2000
P02	.1858	P30	.7897	P81	.5000	P108	.6667
P03	.2138	P31	.2789	P82	.7500	P109	.4300
P04	.0253	P32	.2000	P83	.3750	P110	.7054
P05	.4000	P33	.2000	P84	.2120	P111	.1874
P06	.7537	P34	.5000	P85	.7470	P112	.8950
P07	.5000	P35	.6582	P86	.0400	P113	.4140
P08	.1000	P36	.3333	P87	.0400	P114	.3361
P09	.2810	P37	.3333	P88	.1853	P115	.0023
P10	.6181	P38	.5000	P89	.5000	P116	.6056
P11	.7500	P39	.2687	P90	.1415	P117	.5144
P12	.2000	P40	.1500	P91	.5517	P118	.5113
P13	.1332	P41	.1500	P92	.1200	P119	.9999
P14	.7537	P42	.7897	P93	.4000	Q02	.1885
P15	.8157	P43	.6582	P94	.0640	Q04	.6212
P16	.7537	P44	.5375	P95	.3358	Q07	.7957
P17	.3333	P45	.6758	P96	.4280	Q09	.0000
P18	.3333	P46	.6039	P97	.2608	Q12	.5384
P19	.2004	P62	.4000	P98	.0001	Q14	.3200
P20	.5562	P63	.0463	P99	.6667	Q17	.4197
P21	.8000	P65	.3333	P100	.0001	Q19	.6003
P22	.8000	P67	.1486	P101	.8620	Q22	.0025
P23	.1753	P72	.0634	P102	.3418	Q24	.3986
P24	.4664	P73	.1336	P103	.6248	Q27	.6392
P25	.0001	P77	.0133	P104	.9999	Q29	.1010
P26	.6667	P78	.2058	P105	.7080		
P27	.3953						

‡Scale factors and parameters are in engineering units (U.S. customary units).

REFERENCES

1. Bentz, Charles E.; and Zeller, John R.: Integrated Propulsion Control System Program. SAE Paper 730359, April 1973.

2. Szuch, John R.; and Bruton, William M.: Real-Time Simulation of the TF30-P-3 Turbofan Engine Using a Hybrid Computer. NASA TM X-3106, 1974.

3. Arpasi, Dale J.; Cwynar, Dave S.; and Wallhagen, Robert E.: Sea-Level Evaluation of Digitally Implemented Turbojet Engine Control Functions. NASA TN D-6936, 1972.

4. Cwynar, David S.; and Batterton, Peter G.: Digital Implementation of the TF30-P-3 Turbofan Engine Control. NASA TM X-3105, 1974.

5. Seldner, Kurt; Mihaloew, James R.; and Blaha, Ronald J.: Generalized Simulation Technique for Turbojet Engine System Analysis. NASA TN D-6610, 1972.

6. Koenig, Robert W.; and Fishbach, Laurence H.: GENENG - A Program for Calculating Design and Off-Design Performance for Turbojet and Turbofan Engines. NASA TN D-6552, 1972.

7. Fishbach, Laurence H.; and Koenig, Robert W.: GENENG II - A Program for Calculating Design and Off-Design Performance of Two- and Three-Spool Turbofans with as many as Three Nozzles. NASA TN D-6553, 1972.

8. Sellers, James F.; and Daniele, Carl J.: DYNGEN - A Program for Calculating Steady-State and Transient Performance of Turbojet and Turbofan Engines. NASA TN D-7901, 1975.

9. Szuch, John R.: HYDES - A Generalized Hybrid Computer Program for Studying Turbojet or Turbofan Engine Dynamics. NASA TM X-3014, 1974.

10. Szuch, John R.: Analysis of Integral Lift-Fan Engine Dynamics. NASA TM X-2691, 1973.

11. Shapiro, Ascher H.: The Dynamics and Thermodynamics of Compressible Fluid Flow. Vol. I. Ronald Press Co., 1953.

TABLE I. - DESIGN PARAMETERS

Compressor discharge volume, V_3, m^3	0.0468
Main-combustor volume, V_4, m^3	0.0468
Interturbine volume, $V_{4.1}$, m^3	0.6554
Mixing volume, V_6, m^3	0.8470
Augmentor volume, V_7, m^3	0.7046
Duct volume, V_{13}, m^3	1.426
Augmentor inductance, $(l/Ag_c)_{AB}$, $N\text{-}sec^2/kg\text{-}cm^2$	0.0007598
Duct inductance, $(l/Ag_c)_D$, $N\text{-}sec^2/kg\text{-}cm^2$	0.007598
High-speed-rotor inertia, I_H, $N\text{-}cm\text{-}sec^2$	515.2
Low-speed-rotor inertia, I_L, $N\text{-}cm\text{-}sec^2$	610.0
Main-combustor pressure loss coefficient, K_B, $N^2\text{-}sec^2/cm^4\text{-}K\text{-}kg^2$	0.00165
Low-pressure-turbine discharge pressure loss coefficient, K_{PR5}	1.022
Augmentor pressure loss coefficient, K_{AB}, $N^2\text{-}sec^2/cm^4\text{-}K\text{-}kg^2$	4.3716×10^{-6}
Nozzle flow coefficient, K_N, $kg\text{-}K^{1/2}/N\text{-}sec$	0.1557
Fraction of high-pressure-turbine cooling bleed that performs work, K_{BLWNT}	0.55
Fraction of low-pressure-turbine cooling bleed that performs work, K_{BLWLT}	0.06
Fan inlet specific heat, $c_{p,2}$, J/kg-K	1002
Compressor specific heat, $c_{p,2.2}$, J/kg-K	1003
Compressor discharge specific heat, $c_{p,3}$, J/kg-K	1043
Main-combustor specific heat, $c_{p,4}$, J/kg-K	1147
Interturbine specific heat, $c_{p,4.1}$, J/kg-K	1079
Mixing-volume specific heat, $c_{p,6}$, J/kg-K	1064
Augmentor specific heat, $c_{p,7}$, J/kg-K	1064
Duct inlet specific heat, $c_{p,13'}$, J/kg-K	1004
Duct discharge specific heat, $c_{p,16}$, J/kg-K	1030
Main-combustor specific-heat ratio, γ_4	[a]1.338
Interturbine specific-heat ratio, $\gamma_{4.1}$	1.347
Mixing-volume specific-heat ratio, γ_6	1.381
Augmentor specific-heat ratio, γ_7	[b]1.382
Compressor discharge temperature time constant, τ_3, sec	0.05
Duct temperature time constant, τ_{13}, sec	0.50
Heating value of fuel, HVF, J/kg	4.407×10^7

[a]Effectively decreased by a factor of 20 to match baseline digital data.

[b]Effectively decreased by a factor of 10 to increase simulation stability.

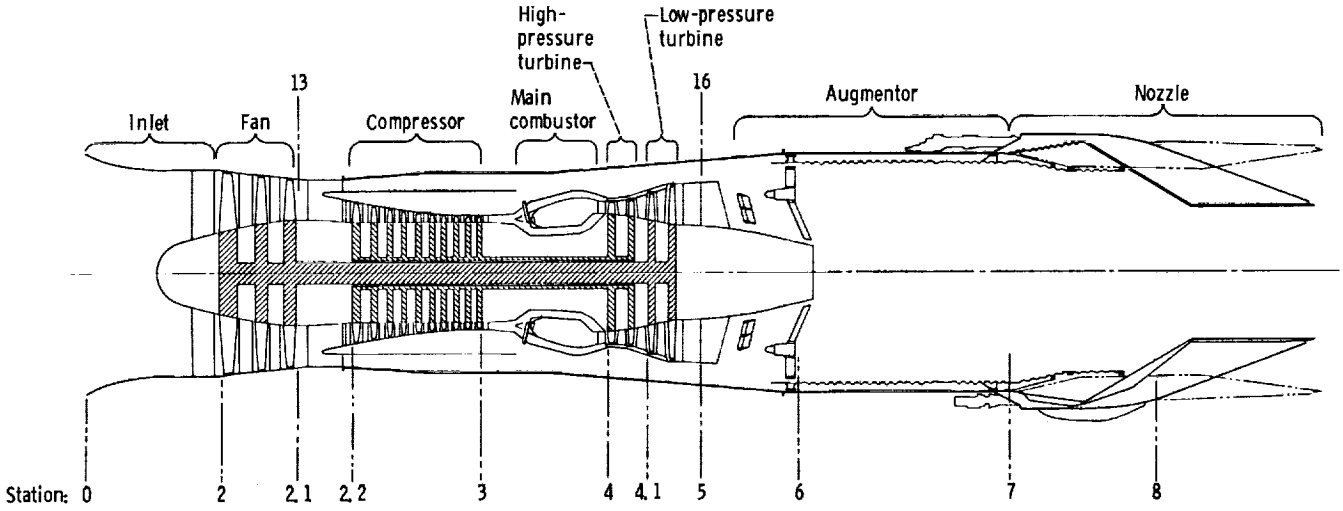

Figure 1. - Schematic representation of F100-PW-100 augmented turbofan engine.

CD-11819-07

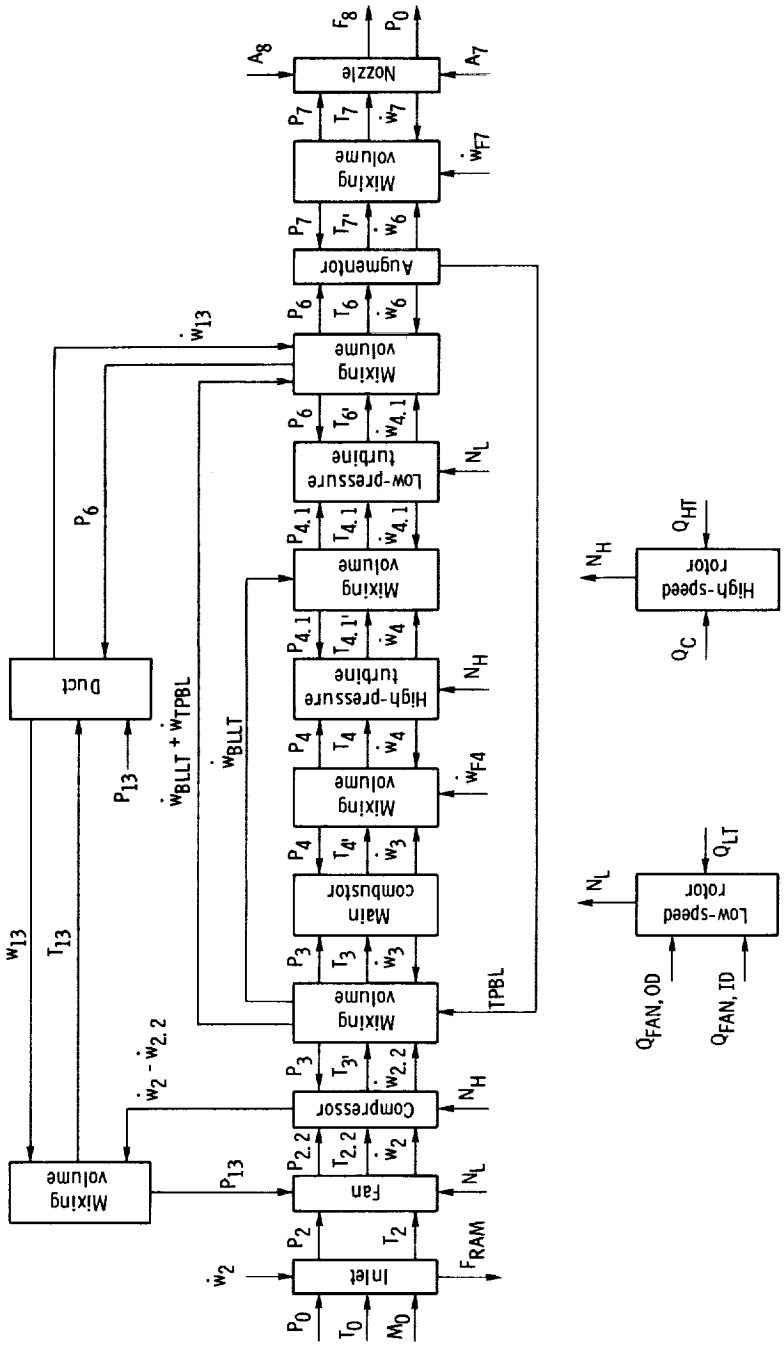

Figure 2. - Computational flow diagram of real-time F100-PW-100 engine simulation.

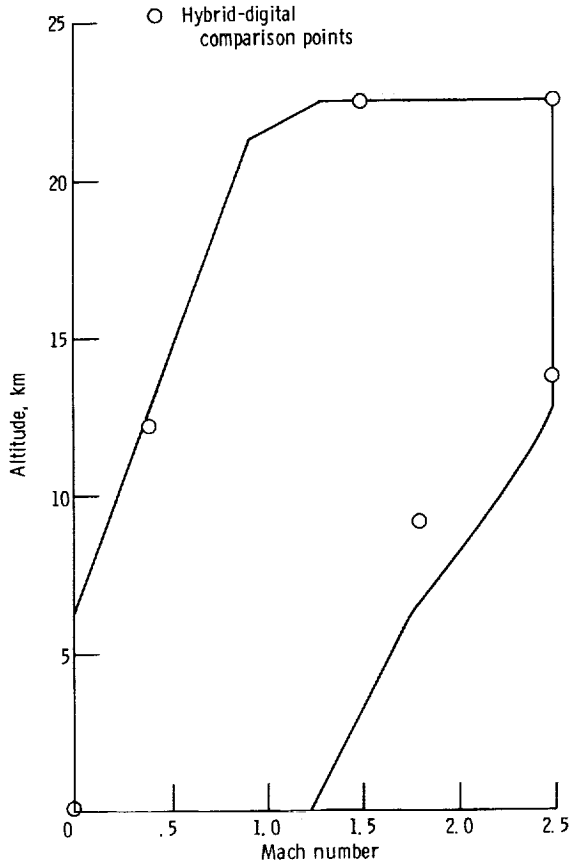

Figure 3. - F100-PW-100 operating envelope.

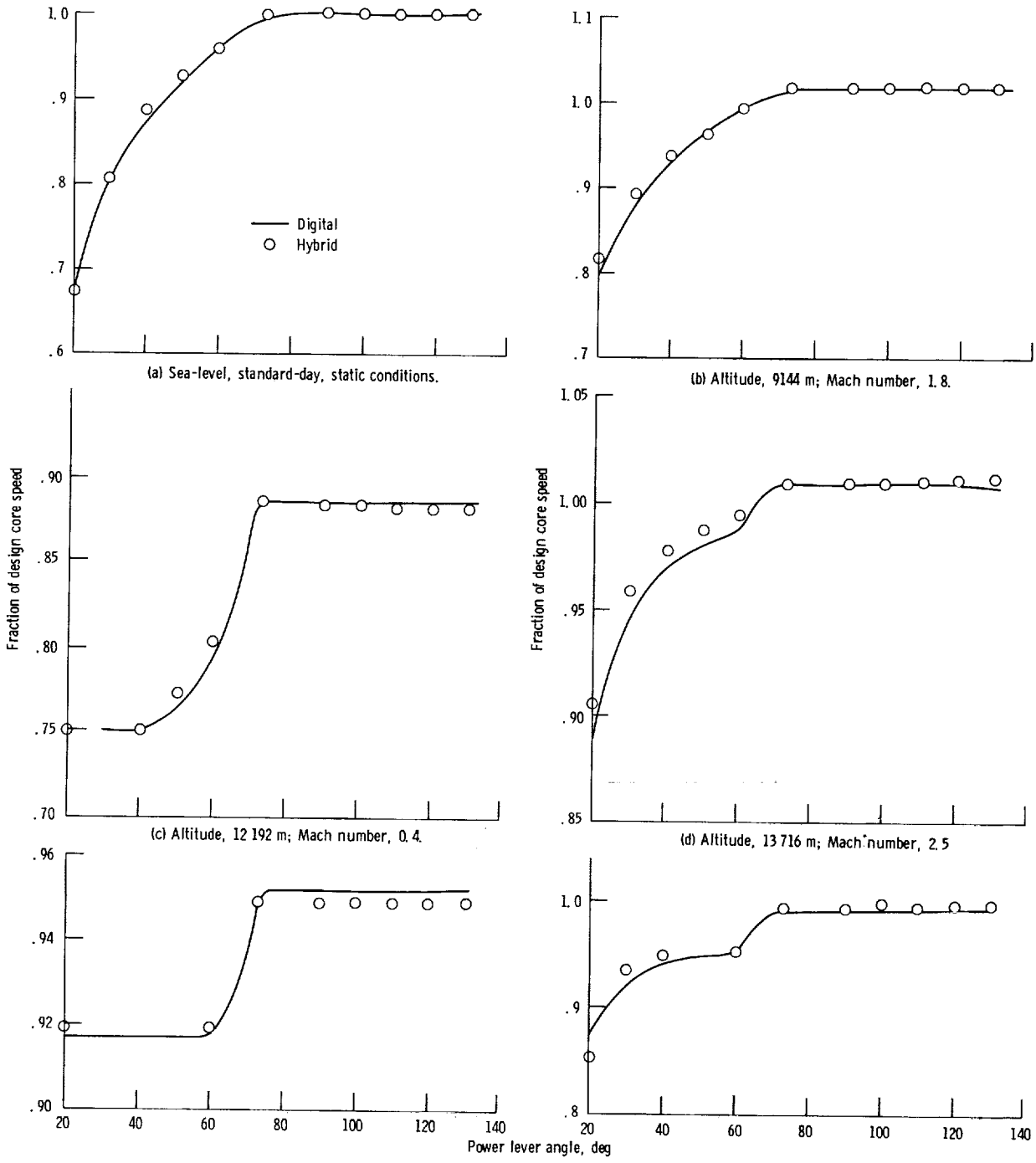

Figure 4. - Comparison of open-loop hybrid and baseline digital steady-state data for core speed.

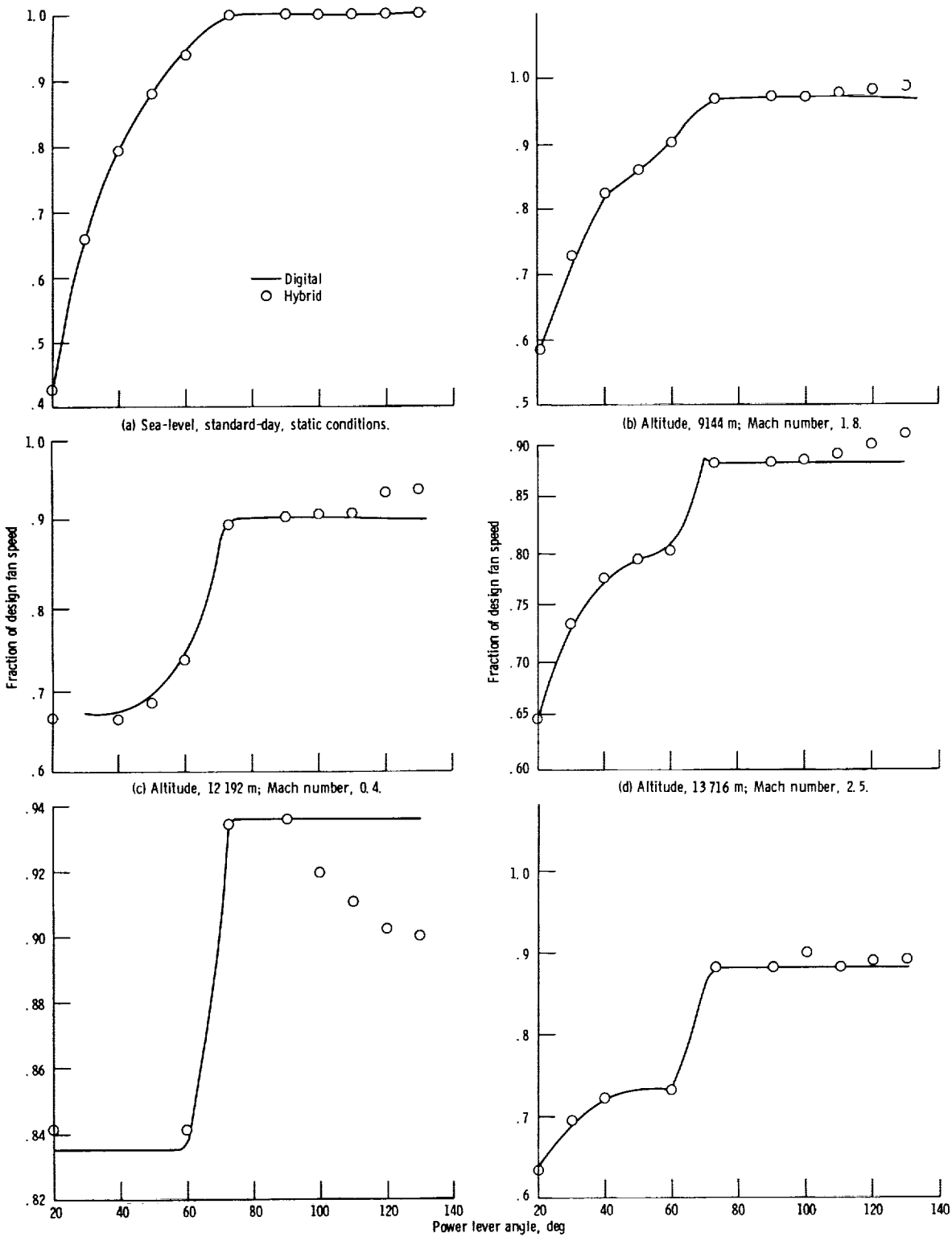

(a) Sea-level, standard-day, static conditions.

(b) Altitude, 9144 m; Mach number, 1.8.

(c) Altitude, 12 192 m; Mach number, 0.4.

(d) Altitude, 13 716 m; Mach number, 2.5.

(e) Altitude, 22 555 m; Mach number, 1.5.

(f) Altitude, 22 555 m; Mach number, 2.5.

Figure 5. - Comparison of open-loop hybrid and baseline digital steady-state data for fan speed.

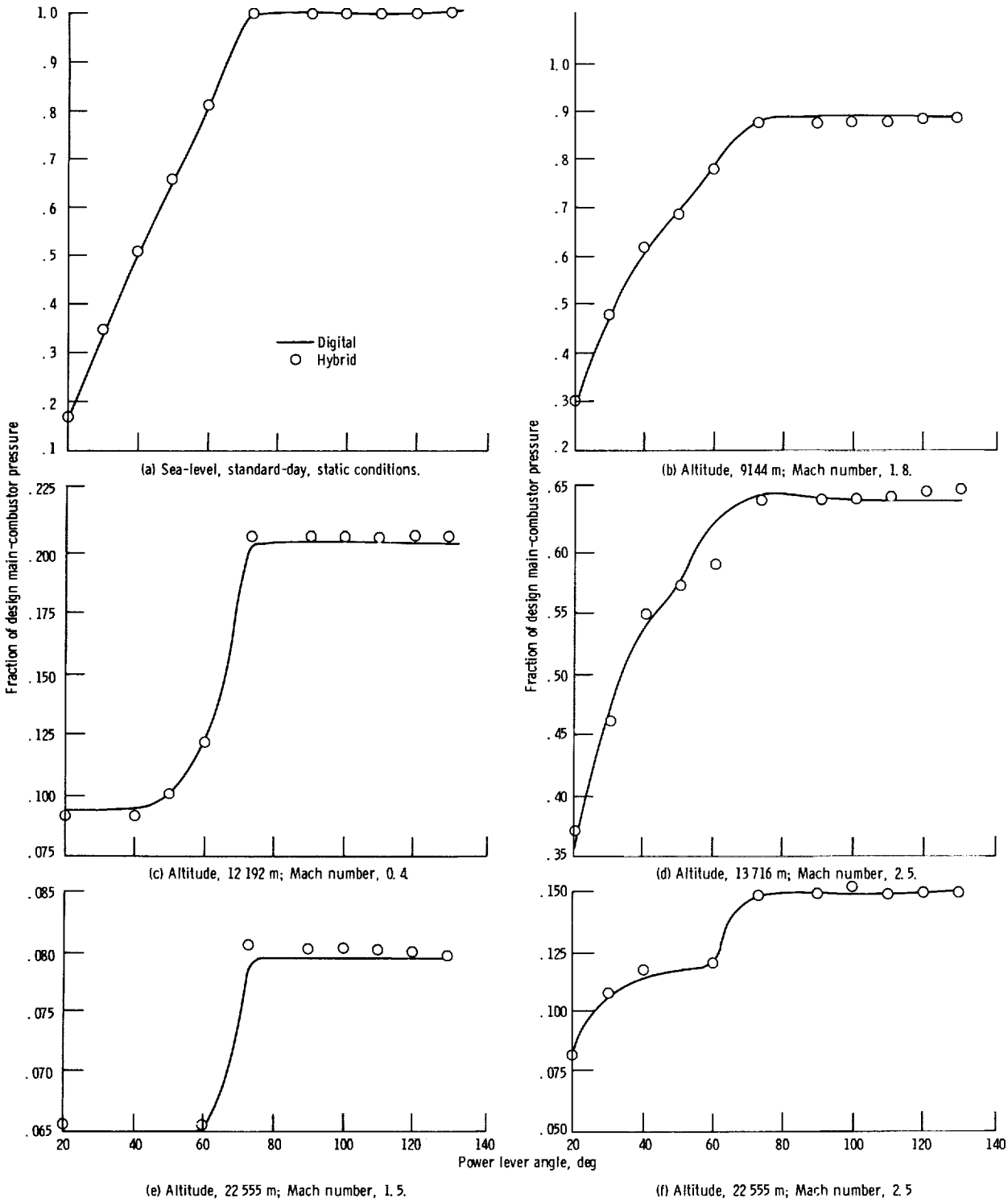

Figure 6. - Comparison of open-loop hybrid and baseline digital steady-state data for main-combustor pressure.

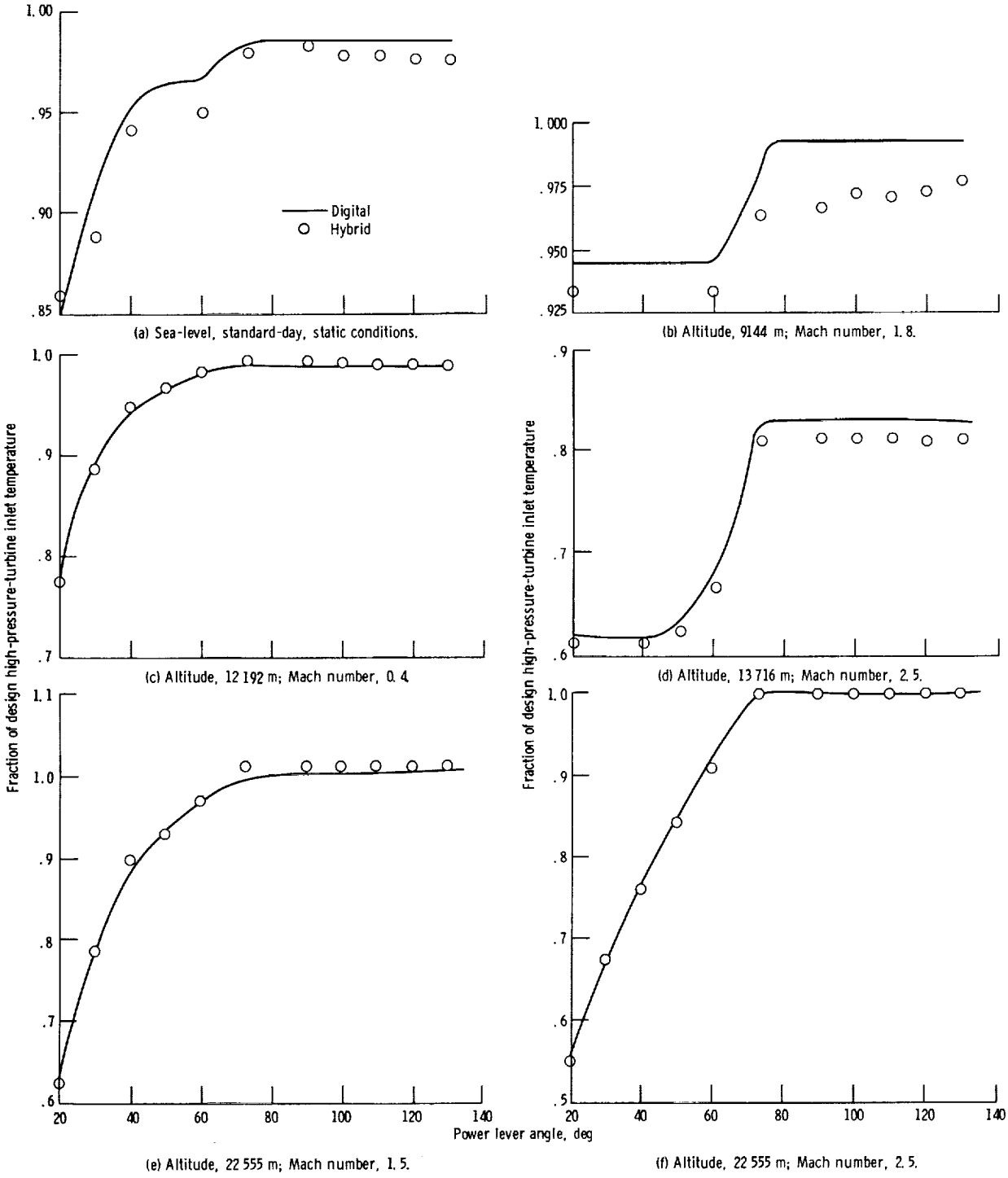

(a) Sea-level, standard-day, static conditions.

(b) Altitude, 9144 m; Mach number, 1.8.

(c) Altitude, 12 192 m; Mach number, 0.4.

(d) Altitude, 13 716 m; Mach number, 2.5.

(e) Altitude, 22 555 m; Mach number, 1.5.

(f) Altitude, 22 555 m; Mach number, 2.5.

Figure 7. - Comparison of open-loop hybrid and baseline digital steady-state data for high-pressure-turbine inlet temperature.

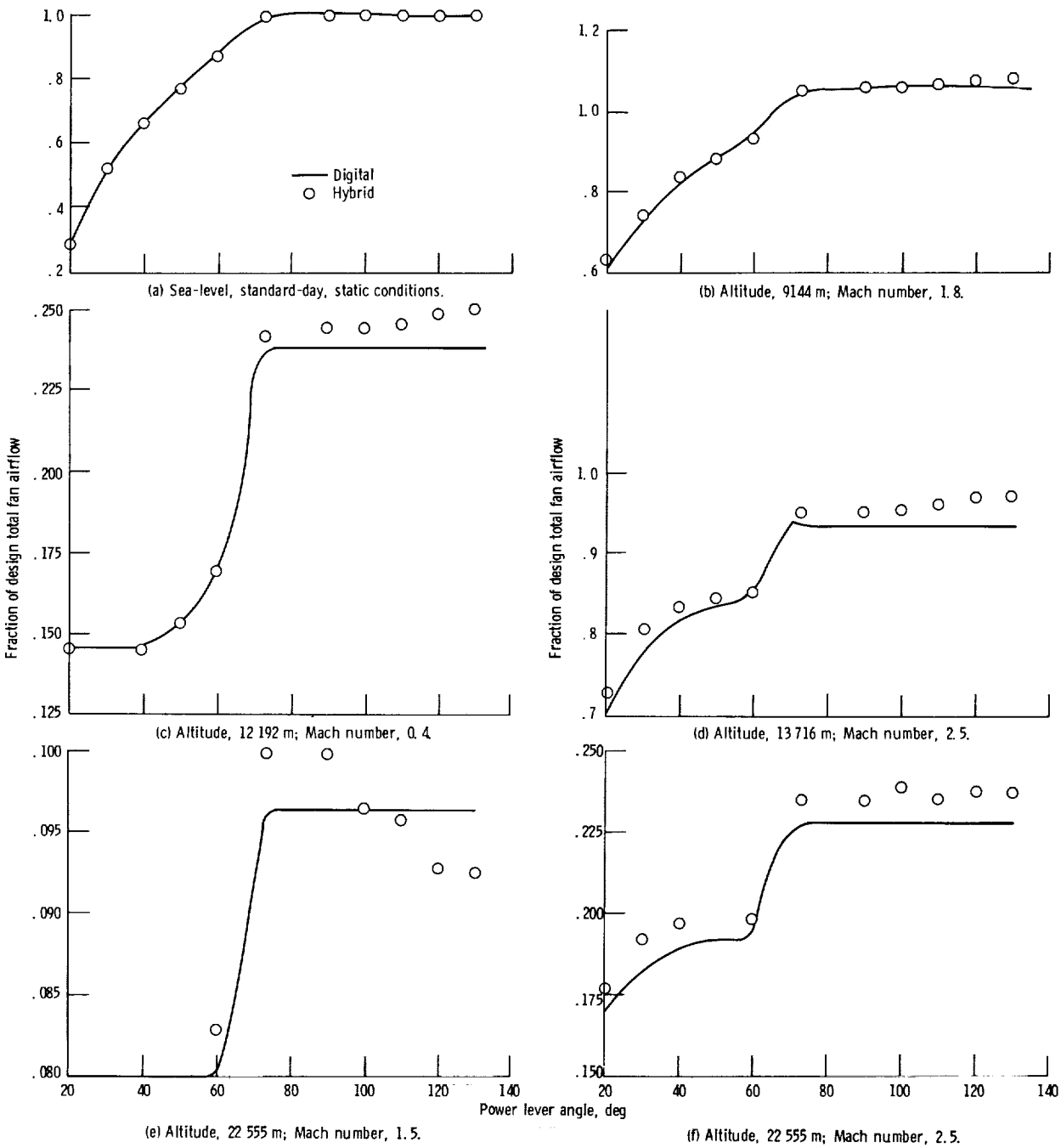

Figure 8. - Comparison of open-loop hybrid and baseline digital steady-state data for fan airflow.

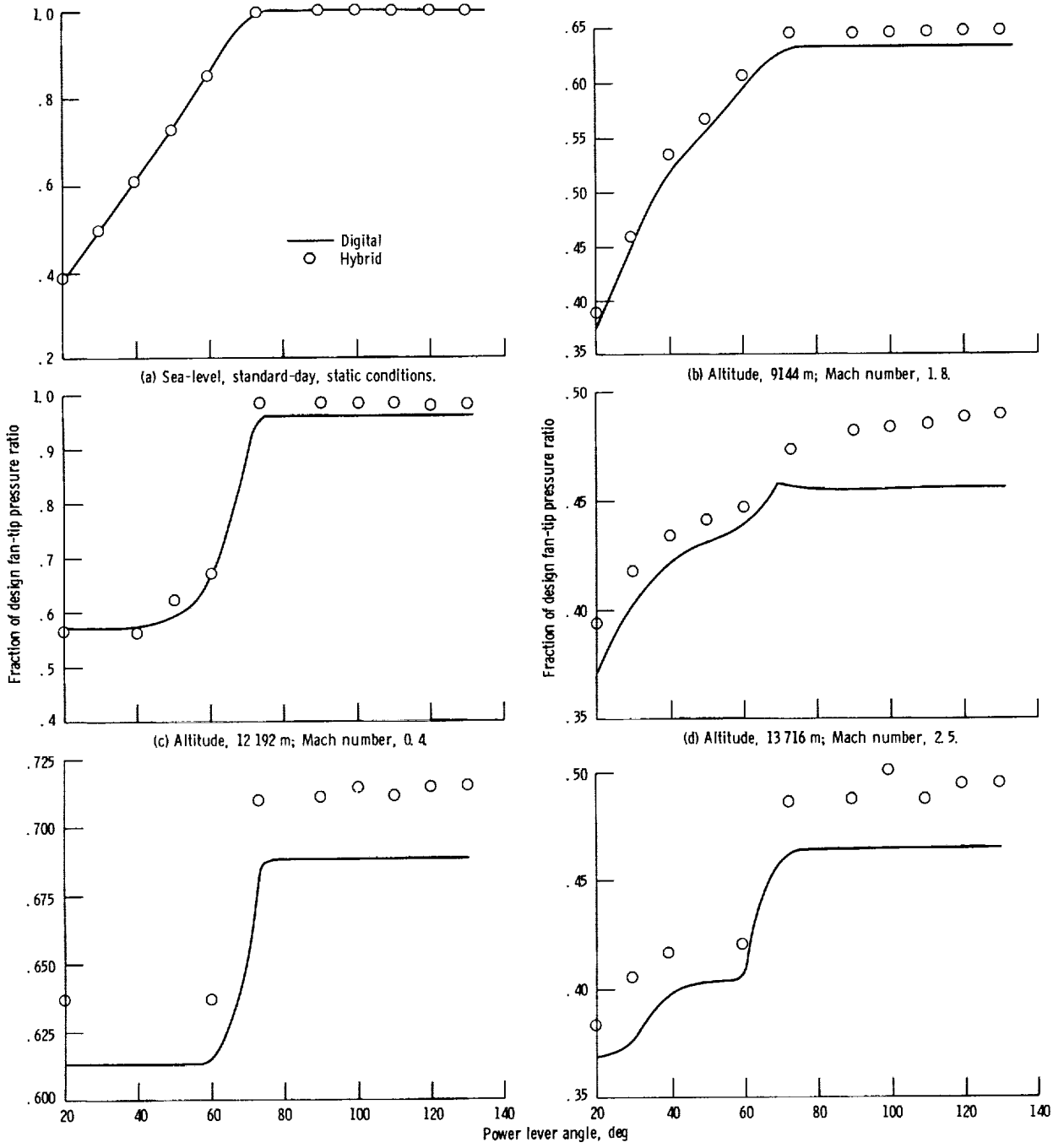

Figure 9. - Comparison of open-loop hybrid and baseline digital steady-state data for fan-tip pressure ratio.

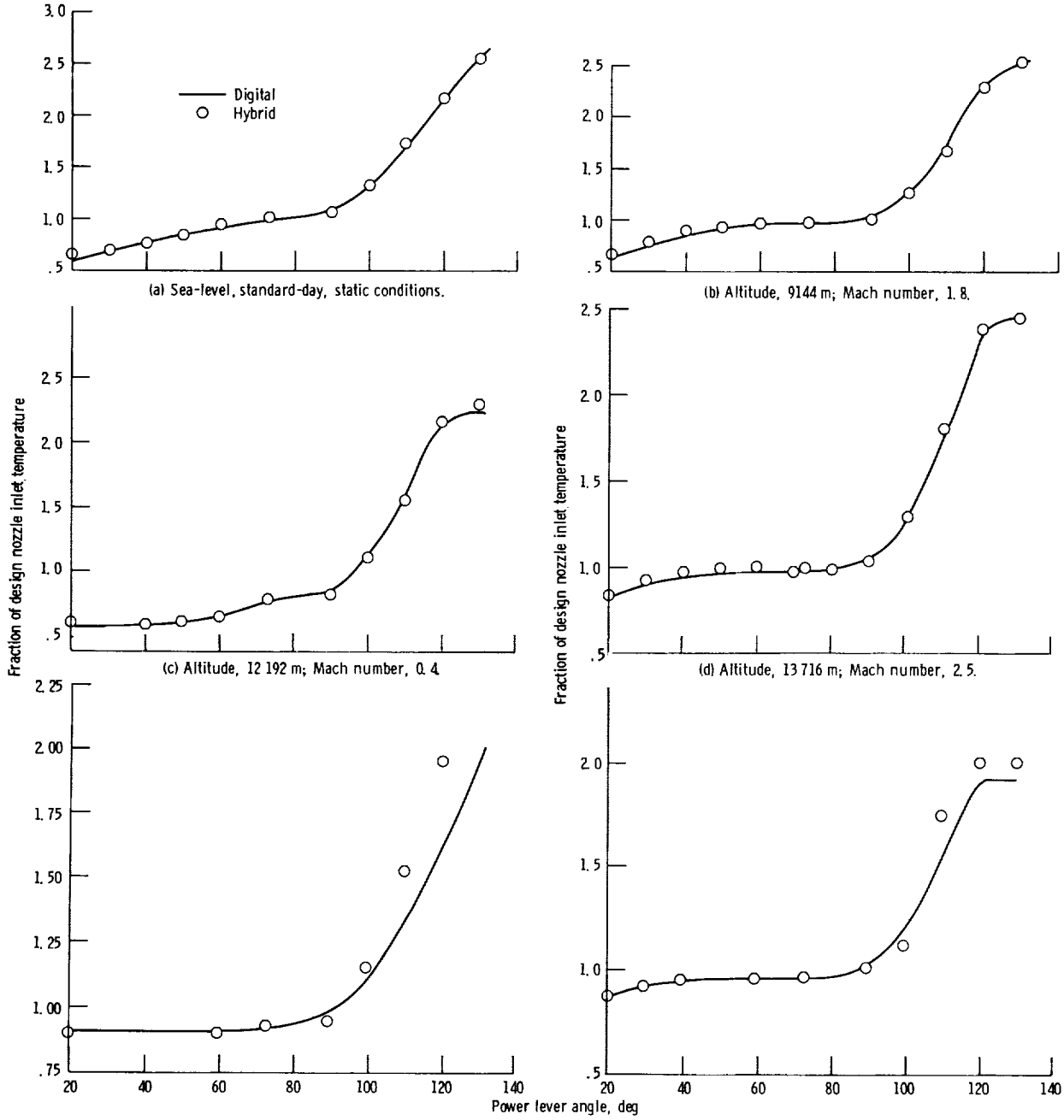

(a) Sea-level, standard-day, static conditions.

(b) Altitude, 9144 m; Mach number, 1.8.

(c) Altitude, 12 192 m; Mach number, 0.4.

(d) Altitude, 13 716 m; Mach number, 2.5.

(e) Altitude, 22 555 m; Mach number, 1.5.

(f) Altitude, 22 555 m; Mach number, 2.5.

Figure 10. - Comparison of open-loop hybrid and baseline digital steady-state data for nozzle inlet temperature.

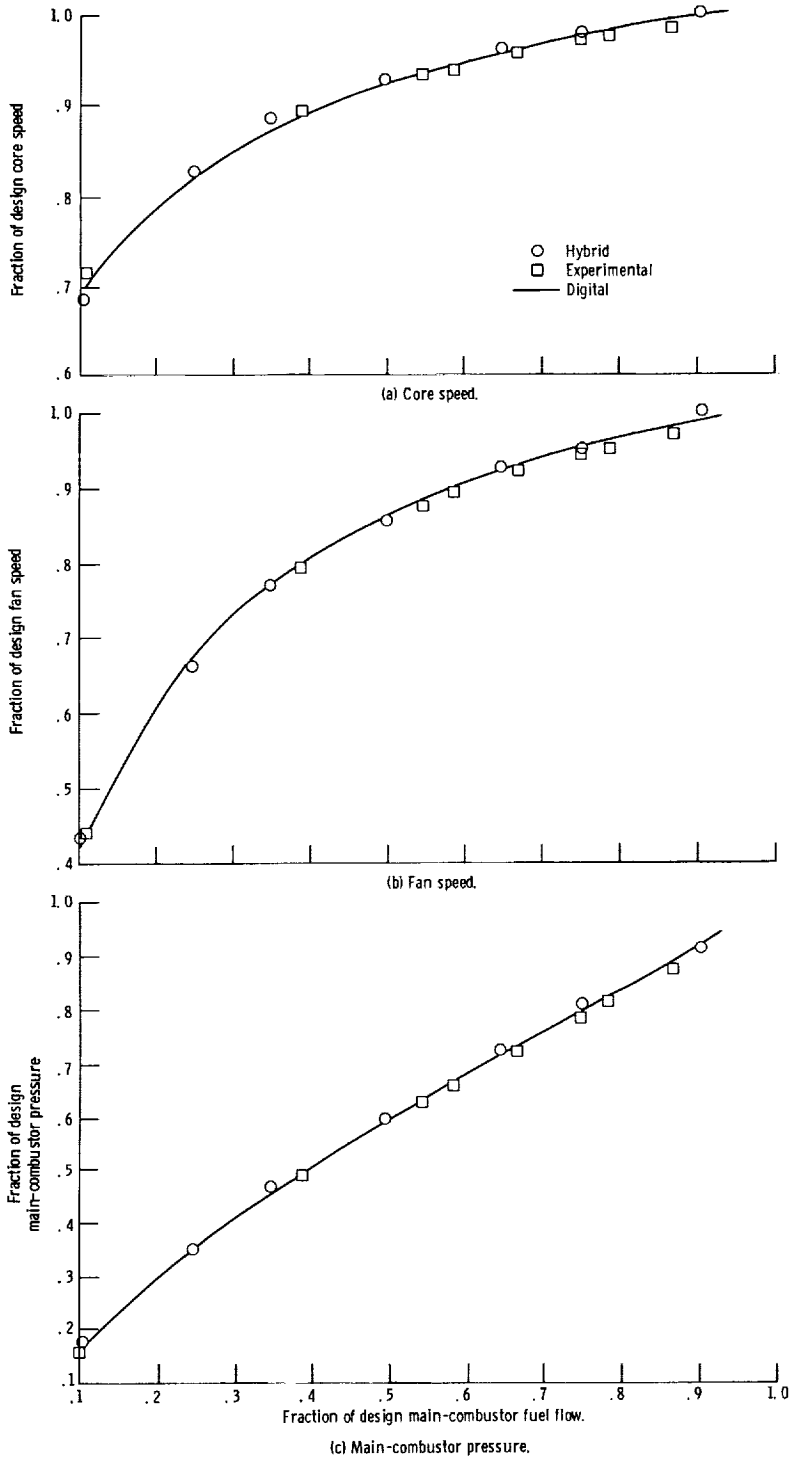

Figure 11. - Comparison of closed-loop hybrid, baseline digital, and experimental steady-state data for nonaugmented mode. Sea-level, static, 297.9 K day conditions.

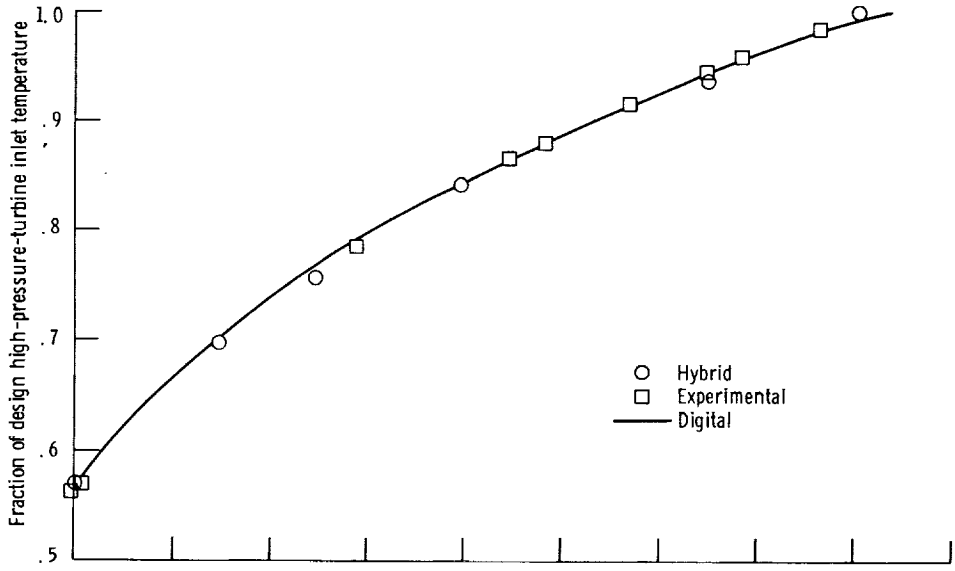

(d) High-pressure-turbine inlet temperature.

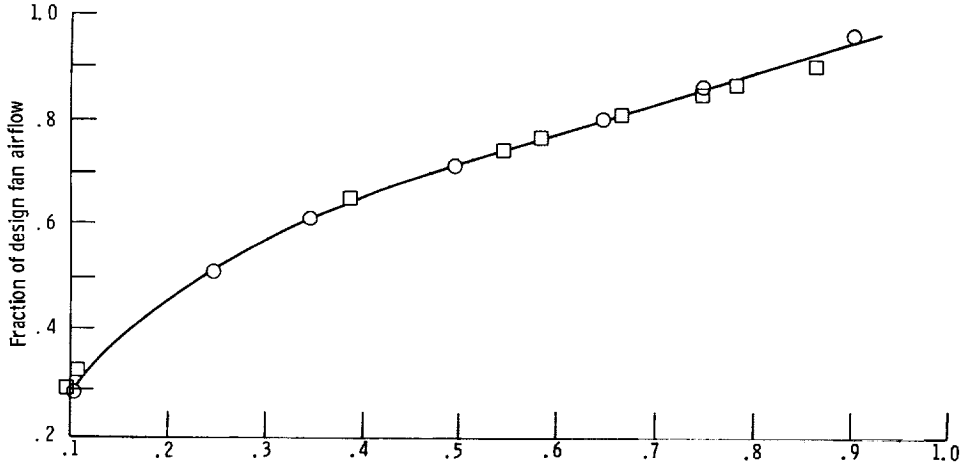

(e) Fan airflow.

Figure 11. - Continued.

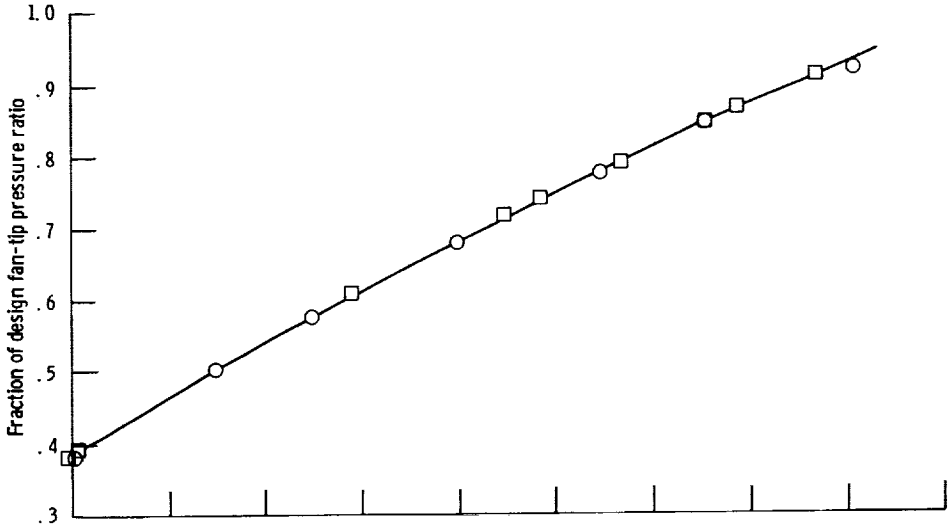

(f) Fan-tip pressure ratio.

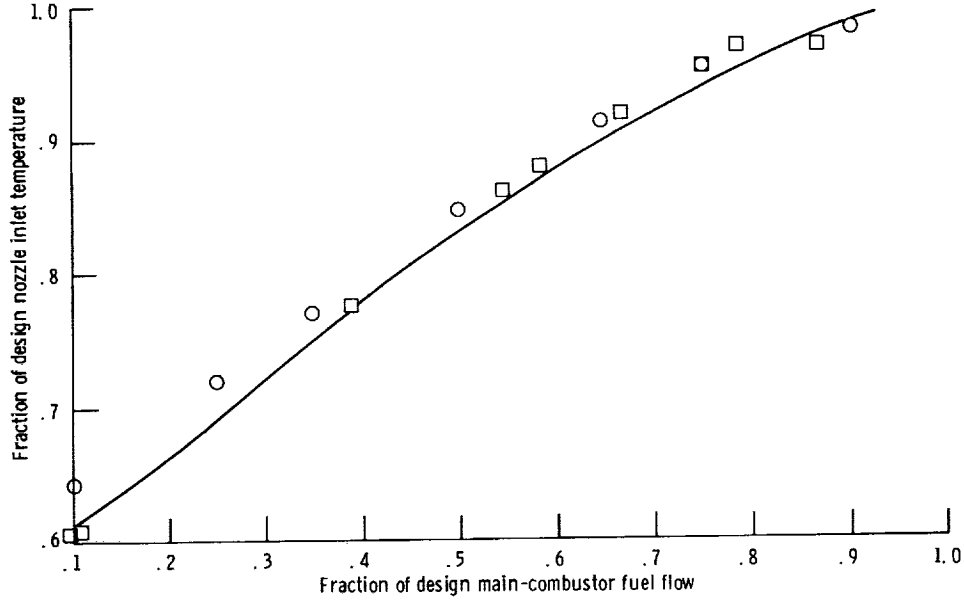

(g) Nozzle inlet temperature

Figure 11. - Concluded.

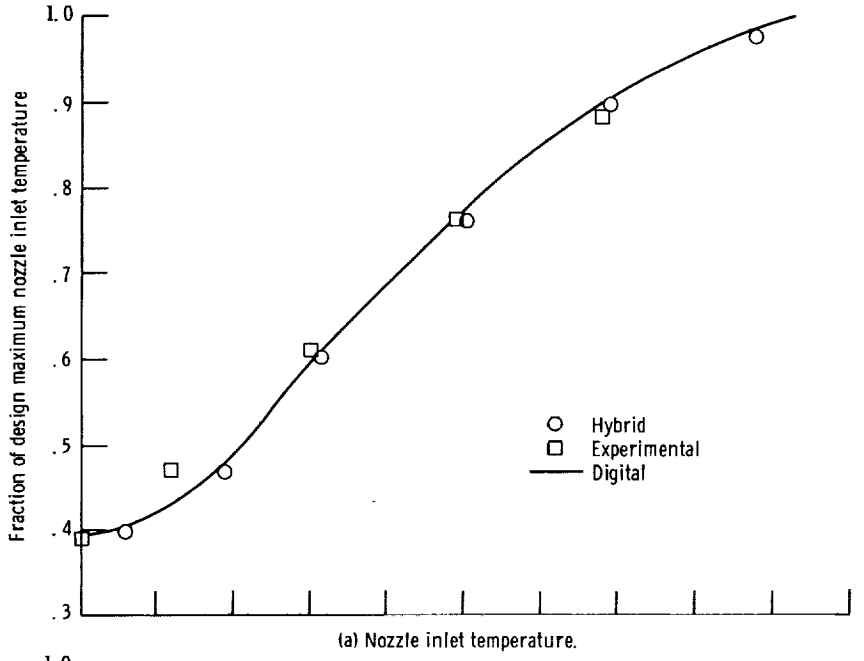

(a) Nozzle inlet temperature.

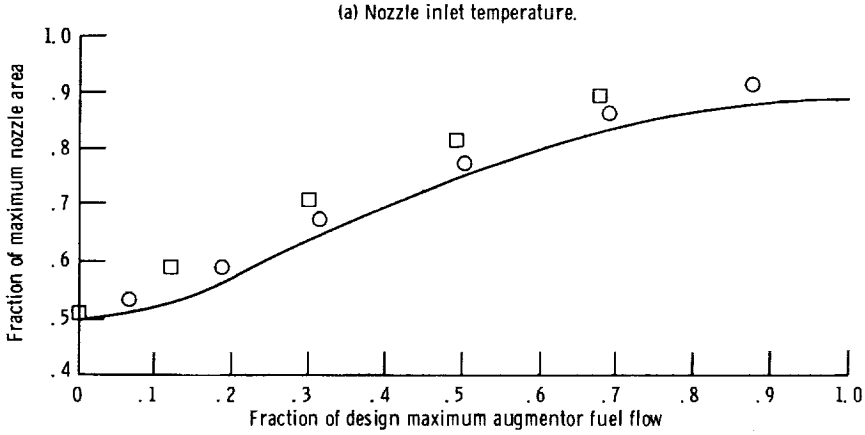

(b) Exhaust nozzle area.

Figure 12. - Comparison of closed-loop hybrid, baseline digital, and experimental data for augmented mode. Sea-level, static, 302.8 K day conditions.

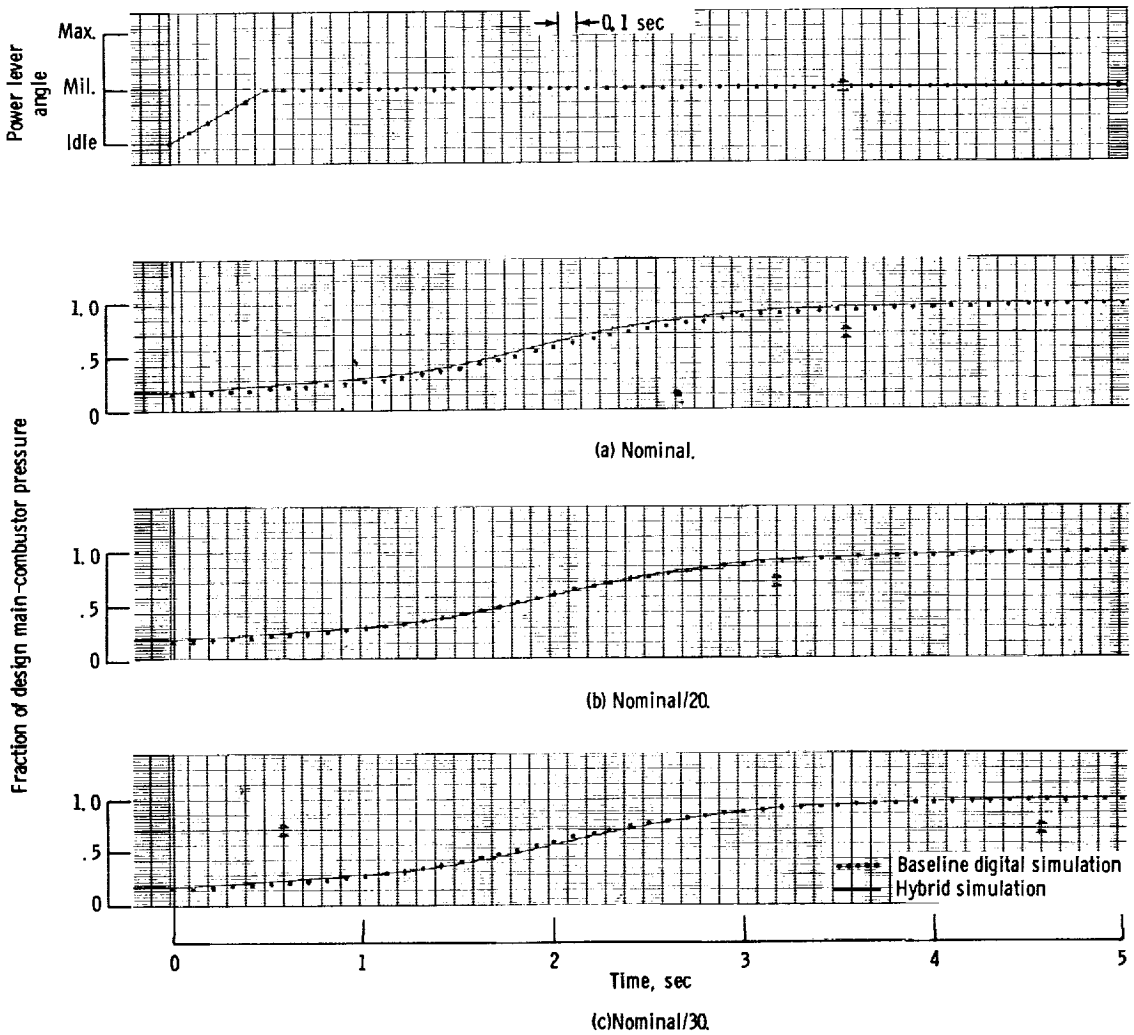

Figure 13. - Effect of main-combustor pressure gain on simulated response of main-combustor pressure to an idle-to-military power lever slam. Idle-area-reset on; sea-level, static conditions.

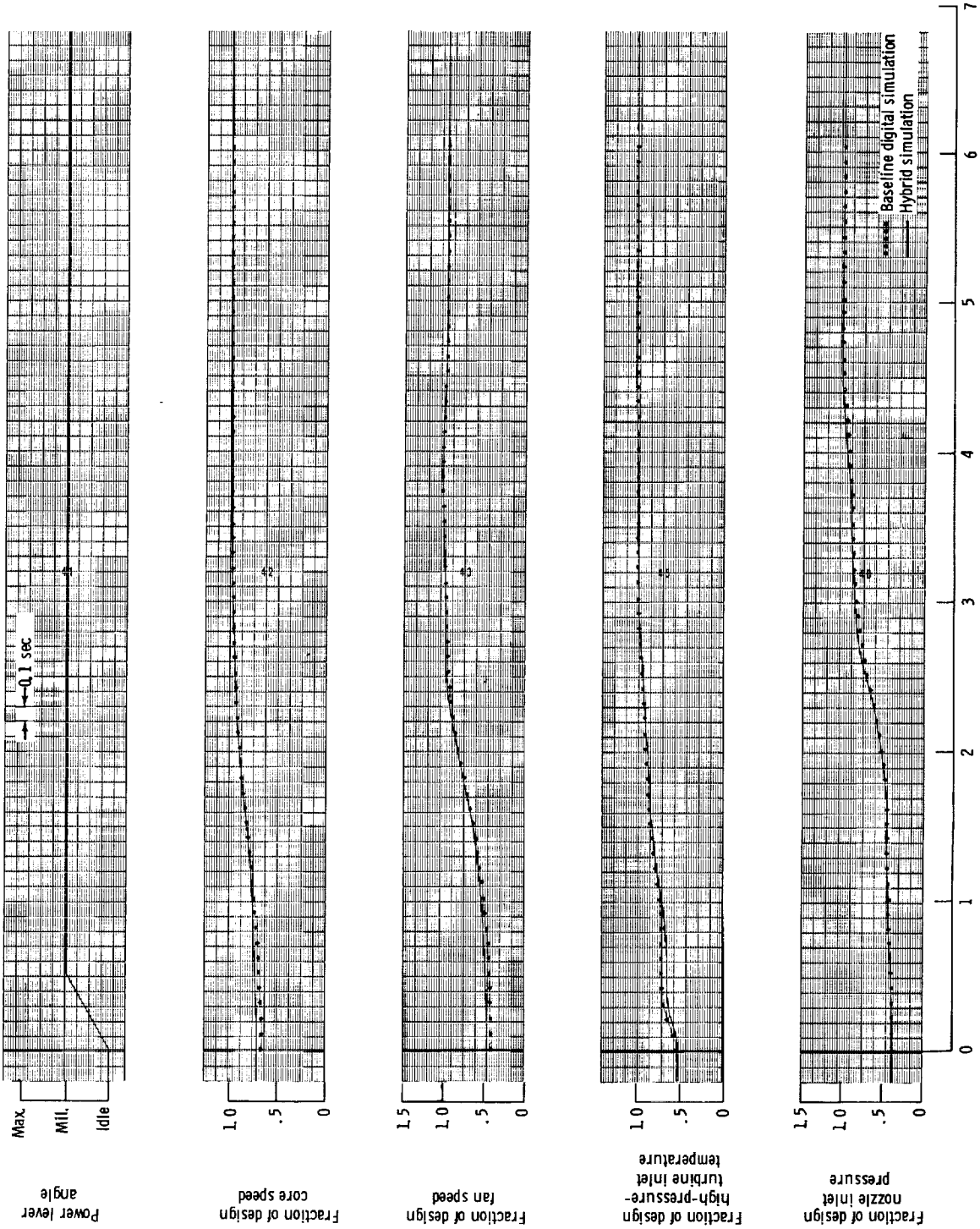

Figure 14. - Comparison of hybrid and baseline digital simulation transient data for idle-to-military power lever slam. Idle-area-reset on; sea-level, static conditions.

Figure 14. - Concluded.

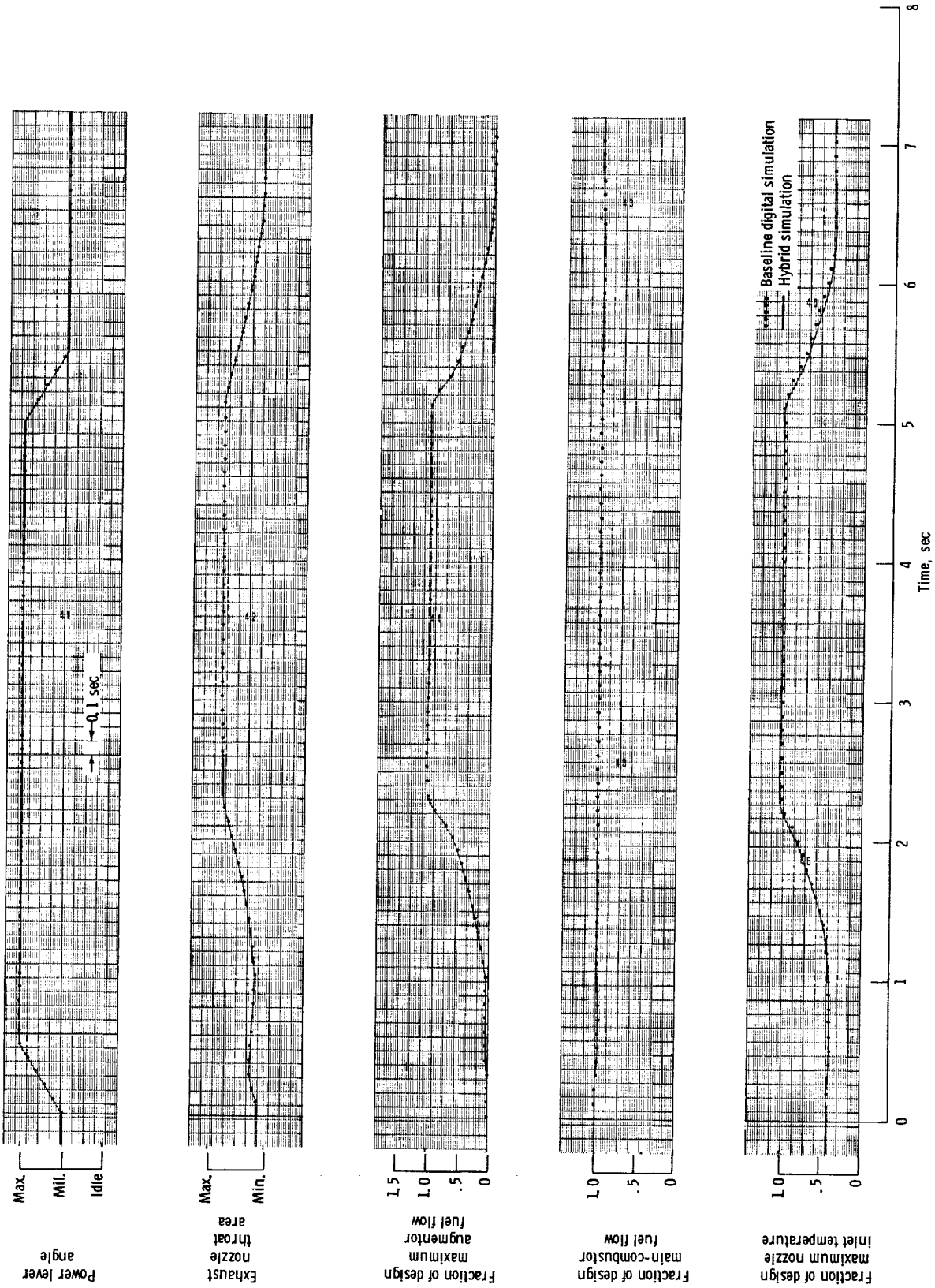

Figure 15. - Comparison of hybrid and baseline digital simulation transient data for military-to-maximum-to-military power lever cycle. Sea-level, static conditions.

Figure 15. - Concluded.

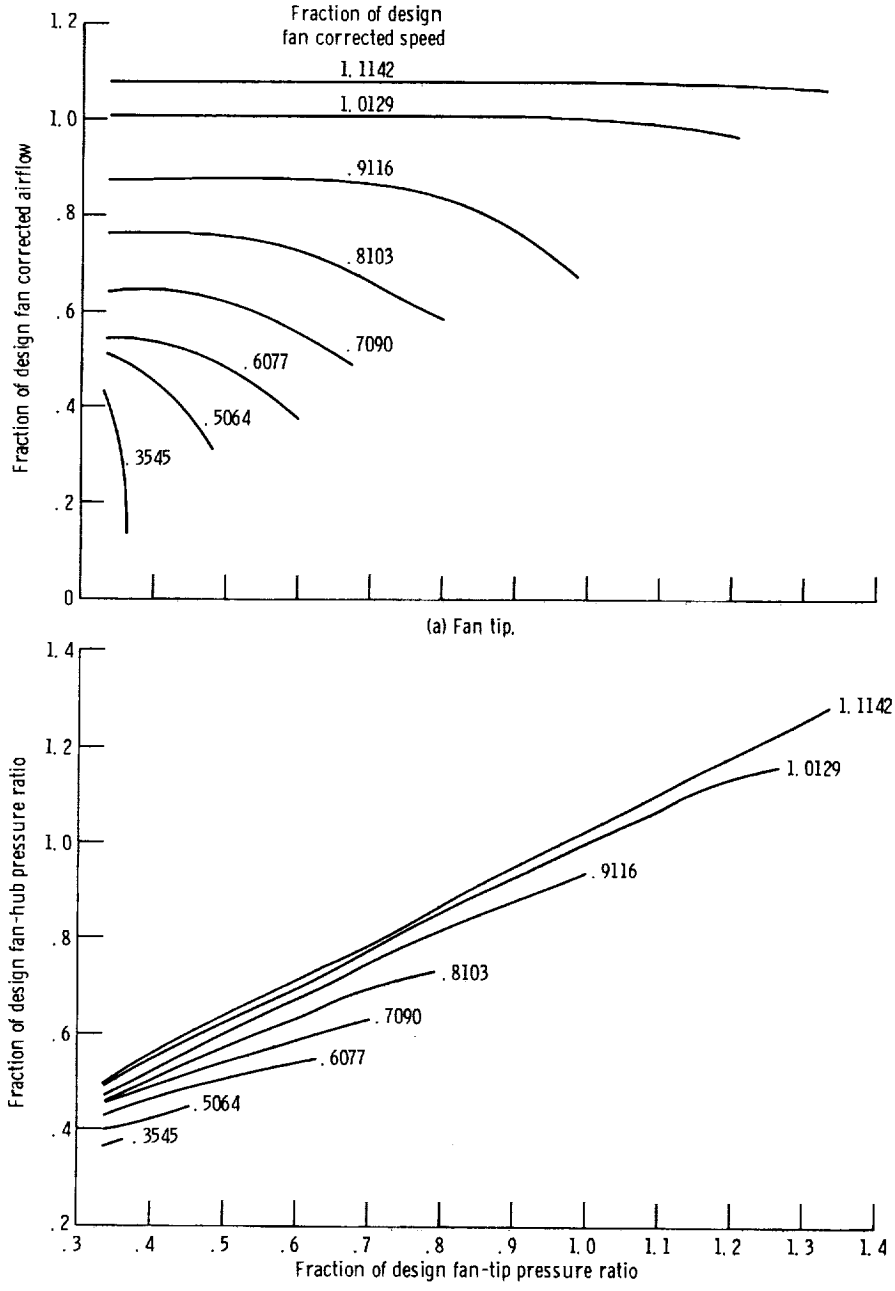

Figure 16. - F100-PW-100 fan performance maps with guide vanes at their axial position (-5.4°).

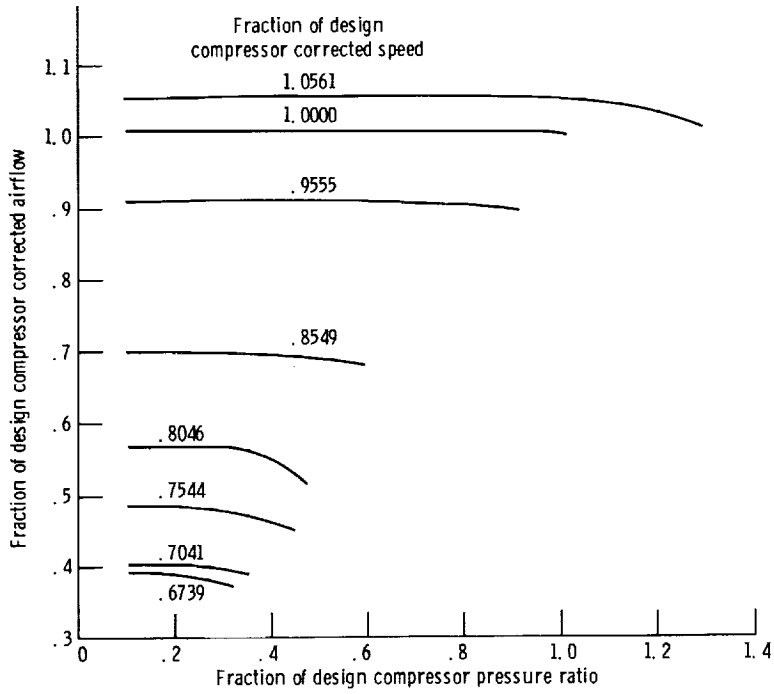

Figure 17. - F100-PW-100 compressor performance map with stator vanes at their axial position (+2.5°).

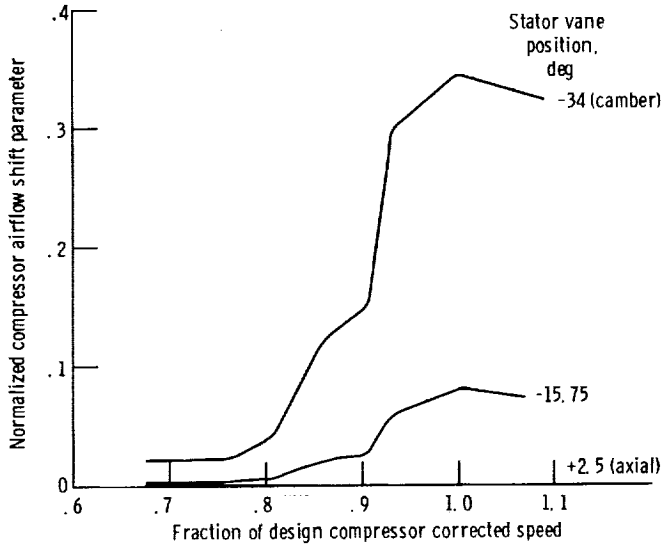

Figure 18. - Effect of variable stator vane position on F100-PW-100 compressor performance map.

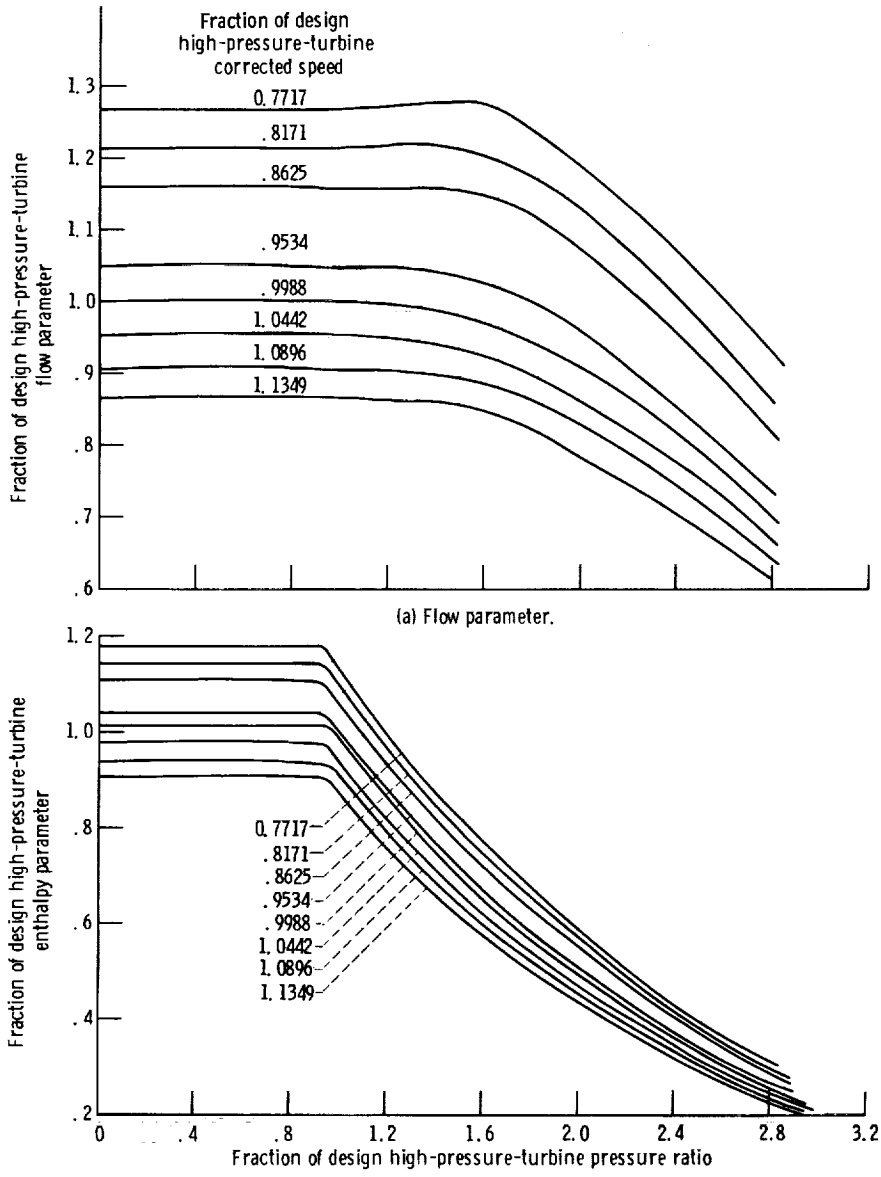

(a) Flow parameter.

(b) Enthalpy drop parameter.

Figure 19. - F100-PW-100 high-pressure-turbine performance maps.

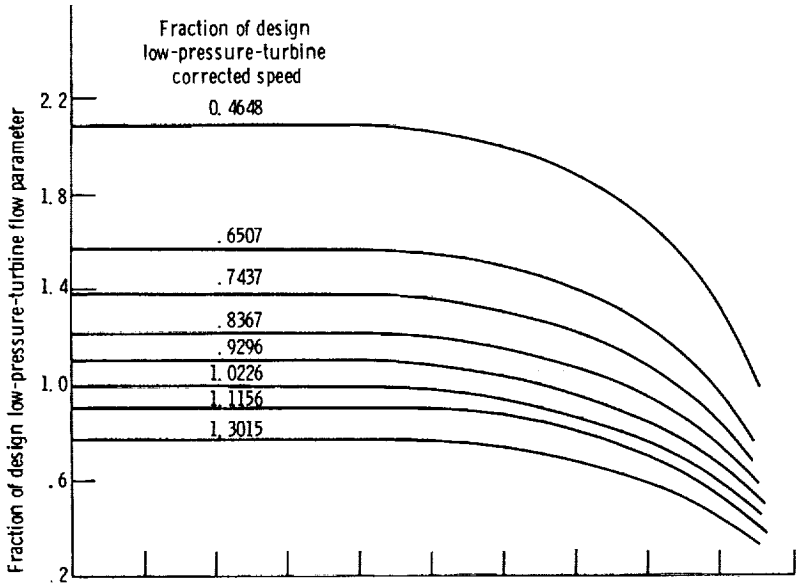

(a) Flow parameter.

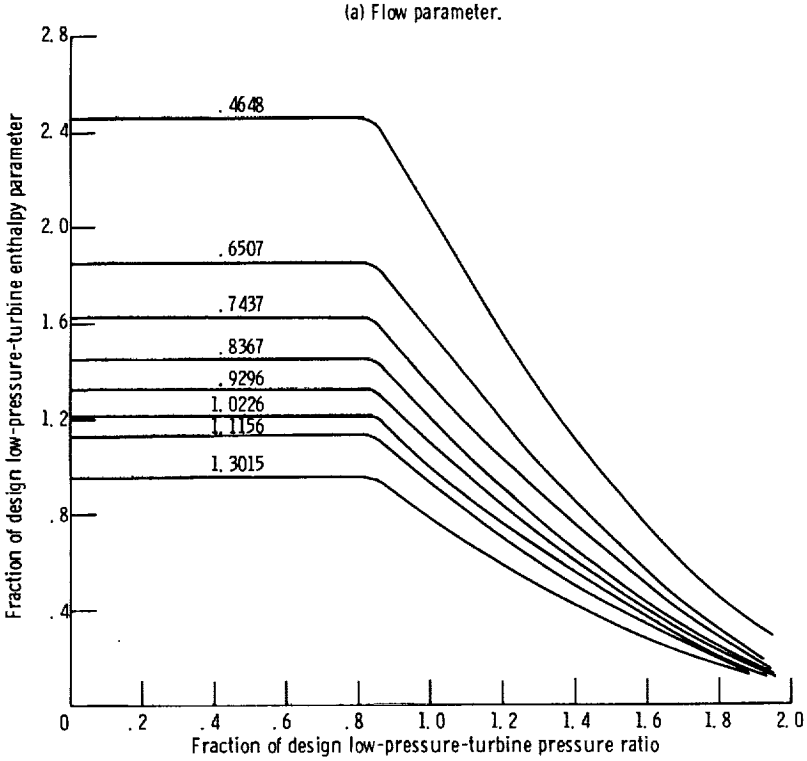

(b) Enthalpy drop parameter.

Figure 20. - F100-PW-100 low-pressure-turbine performance maps.

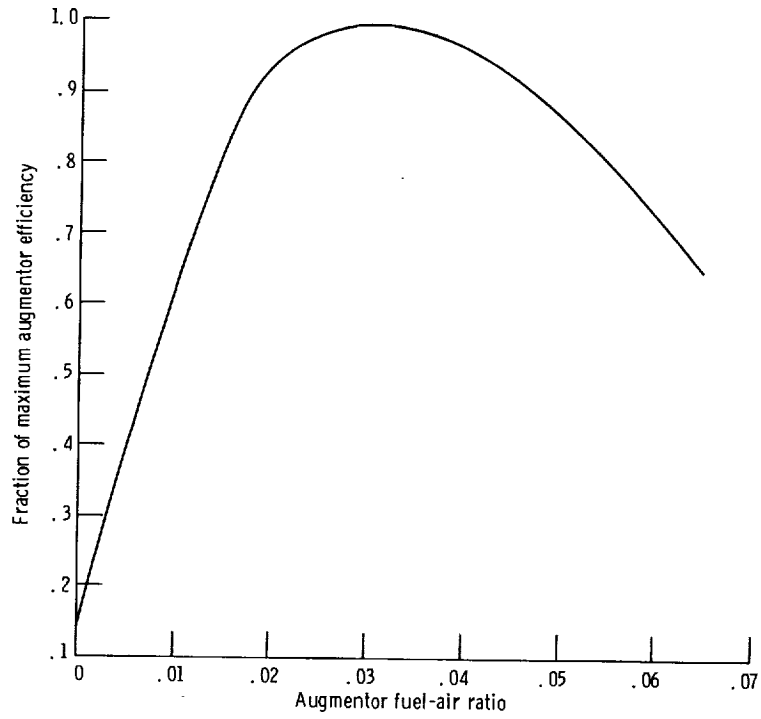

Figure 21. - F100-PW-100 augmentor efficiency map.

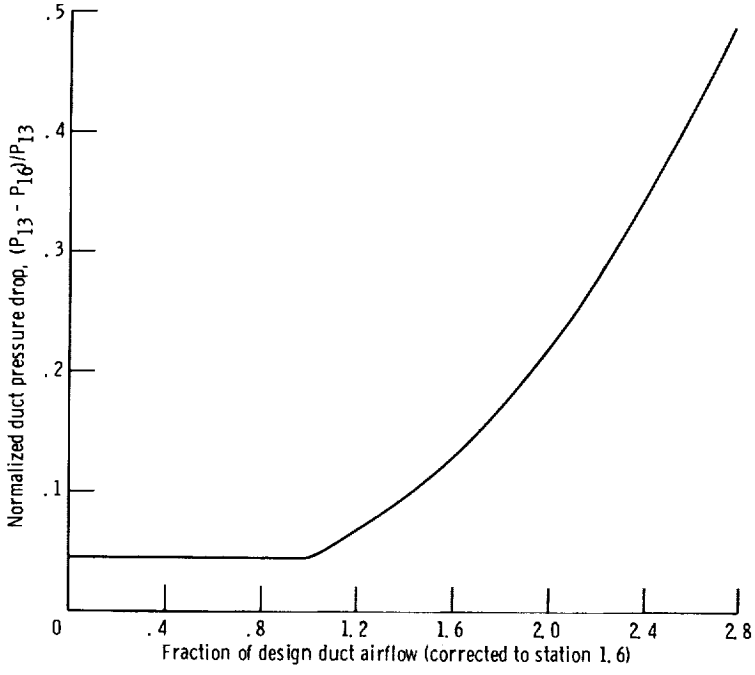

Figure 22. - F100-PW-100 duct pressure loss characteristic.

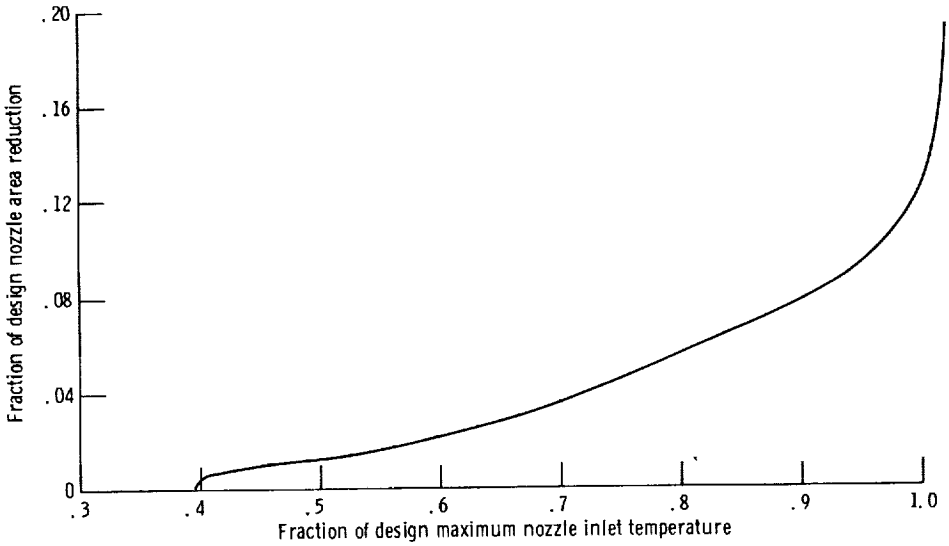

Figure 23. - F100-PW-100 nozzle area reduction required to match baseline sea-level, static augmentor data.

NASA-Langley, 1975 E-8136